



Bridgewater State University

Virtual Commons - Bridgewater State University

Honors Program Theses and Projects


Undergraduate Honors Program

5-14-2019

Synthesis of a Protein Based Photocatalytic Hydrogen Production System

Alexander M. Brown
Bridgewater State University

Follow this and additional works at: https://vc.bridgew.edu/honors_proj

 Part of the [Chemistry Commons](#)

Recommended Citation

Brown, Alexander M.. (2019). Synthesis of a Protein Based Photocatalytic Hydrogen Production System. In *BSU Honors Program Theses and Projects*. Item 355. Available at: https://vc.bridgew.edu/honors_proj/355

Copyright © 2019 Alexander M. Brown

This item is available as part of Virtual Commons, the open-access institutional repository of Bridgewater State University, Bridgewater, Massachusetts.

Synthesis of a Protein Based Photocatalytic Hydrogen Production System

Alexander M. Brown

Submitted in Partial Completion of the
Requirements for Departmental Honors in Chemistry

Bridgewater State University

May 14th, 2019

Dr. Sarah Soltau, Thesis Advisor

Date

Dr. Saritha Nellutla, Committee Member

Date

Dr. Steven Haefner, Committee Member

Date

Abstract

Anthropogenic climate change is one of the most pressing challenges facing humans today. It is scientifically established that the production of copious amounts of greenhouse gases such as carbon dioxide (CO₂) is the primary cause of global warming. Many of these greenhouse gases are produced from the combustion of carbon-based fuels and researchers are investigating promising alternative fuel sources such as hydrogen gas. Hydrogen gas is a clean burning fuel that stores a significant amount of chemical potential energy. The goal of this project was to synthesize a protein based photocatalytic hydrogen production system and to characterize the effects of modifications on the system. Significant progress has been made in developing/synthesizing all of the components of a three-part photocatalytic system including the photosensitizer, [Ru(4-CH₂Br-4'-(2,2'-bipyridine)(2,2'-bipyridine)₂](PF₆)₂, the protein rubredoxin, and a newly designed hydrogen evolution catalyst [Cp*Ir(4,4'-dimethyl-2,2'-bipyridine)Cl]⁺ designed to link to proteins. Preliminary characterization of hydrogen production was determined using a standard curve to detect hydrogen by gas chromatography. Tris(bipyridine)ruthenium(II) in conjunction with a free cobaloxime catalyst was used to analyze the integrity of the analytical method. Future work will allow researchers to attach [Cp*Ir(4,4'-dimethyl-2,2'-bipyridine)Cl]⁺ to a protein linker and test its effectiveness for photochemical hydrogen production which will serve as a standard baseline for future hydrogen production experimentation.

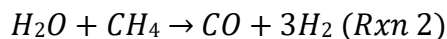
Introduction

As human society passed through the industrial revolution we began producing excessive amounts of greenhouse gases such as carbon dioxide, methane, nitrous oxide, and chlorofluorocarbons. In abundance these gases pervade the atmosphere locking heat onto the surface of the earth and raising global temperatures. Perhaps the most efficient greenhouse gas, carbon dioxide, is a direct product of the combustion of carbon-based fuels. Following the United Nations decision to take action against climate change during the Paris Global Climate Agreement, global warming has become recognized as an international crisis. The United States of America is a major producer of carbon dioxide with over 6,000 metric tons of carbon dioxide being produced from the combustion of fossil fuels in 2016 alone.^{1,2} The inordinate dependence on fossil fuels has pressed scientists to seek out viable alternative energy sources. As hydrogen gas (H₂) is clean burning and stores a tremendous amount of energy in its covalent bond (140MJ/kg) it has become a strong potential candidate to replace fossil fuels.^{1,3} Hydrogen gas can be produced by the reduction of protons through the following half reaction (Reaction 1).



The clear majority of modern industrial practices produce hydrogen gas through steam-methane reformation in which water acts as a reducing agent. In this process, high pressure steam is introduced to methane in the presence of a catalyst to form carbon monoxide and hydrogen gas (Reaction 2). With a separate catalyst, the carbon monoxide is then reacted with water in a water-gas shift reaction (Reaction 3) to produce carbon dioxide and hydrogen gas.⁴ Ultimately this method of producing hydrogen gas requires a large amount of energy, necessitates expensive

catalysts, and produces significant amounts of carbon dioxide. Therefore, it is necessary to form a sustainable standpoint and investigate other methods of producing hydrogen gas.



Recent efforts in producing hydrogen gas have shifted to the attachment of molecular hydrogen evolution catalysts to a light sensitive compound called a photosensitizer through a linker as outlined in Figure 1.⁵ In this system, irradiation in the UV-visible region promotes excitation of electrons on the photosensitizer. As the electrons relax they are transferred to the linker and ultimately to molecular orbitals localized on the catalyst. Following proton collision with the catalyst, the catalyst acts as a reducing agent promoting the formation of hydrogen gas. A sacrificial electron donor provides electrons to the photosensitizer and the cycle continues. As the efficiencies of such complexes are highly dependent on the synergy of the components it is critical to understand the role each individual piece plays in order to develop complexes with higher turnover rates.



Figure 1. Schematic of a typical linked hydrogen evolution complex. In such a system, the PS represents a light-absorbing molecule called a photosensitizer and the Cat represents a hydrogen evolution catalyst.

Photosensitizer

The role of a photosensitizer in a photocatalytic hydrogen production system is to translate photonic energy into electric potential, passing electrons to the linker and reducing the hydrogen evolution catalyst. A typical organic photosensitizer is composed of a large pi conjugated system, ultimately lowering the energy gap between the highest occupied molecular orbital (HOMO) and the lowest occupied molecular orbital (LUMO) into the UV-Visible range (**Figure 2**). Excitation of the HOMO electrons allows for subsequent transfer from a singlet state to unoccupied adjacent molecular orbitals on neighboring atoms.⁶

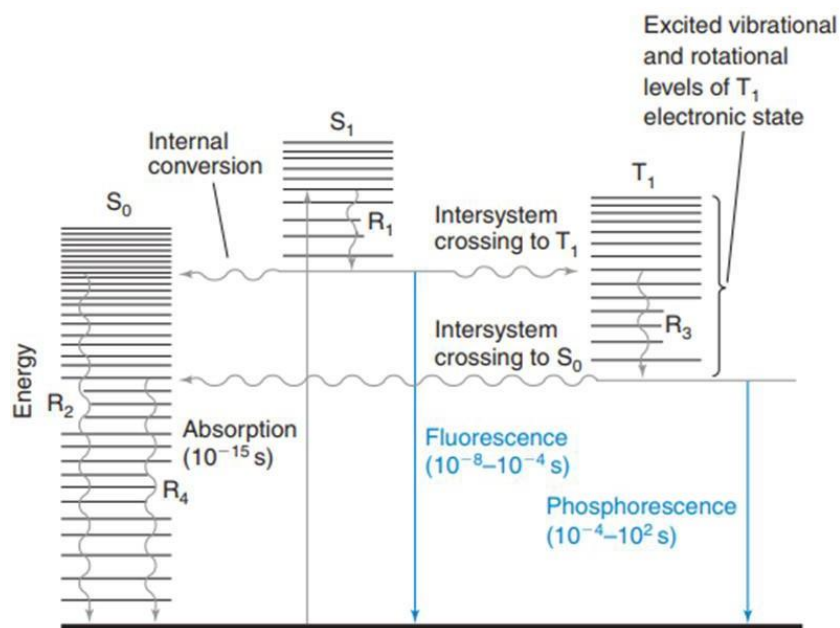


Figure 2. Simplified molecular orbitals of a pi conjugated system. Excitation results in electron migration to the LUMO and relaxation to adjacent molecular orbitals through intersystem crossing. Adapted from Harris's *Quantitative Chemical Analysis*.⁶

A major driving force behind the synthesis of novel organic photosensitizers came from their use in photodynamic cancer treatment after it was discovered that these compounds catalyzed the formation of reactive oxygen species *in vivo*.^{7,8} The introduction of penetrative radiation at the

tumor site catalyzes the formation and presence of reactive oxygen species to promote cell death centered around the tumor.^{7, 8} One of the first photodynamic therapeutic agents and a classical example of an organic photosensitizer is photofrin (Figure 3). Today, a large number of photosensitizer-based cancer therapeutics are available on the market or are in clinical trials. Stemming in part of the success from the use of photosensitizers as phototherapeutic agents, research began to shift to investigating their potential use in photocatalytic systems in conjugation with catalysts designed for carbon dioxide reduction or promoting the hydrogen evolution reaction.

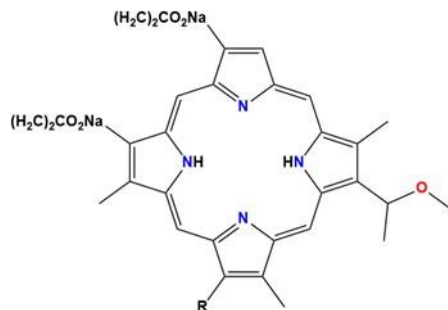


Figure 3. Chemical structure of Photofrin an established photodynamic cancer therapeutic agent.

One of the first organic dyes to demonstrate viable quantum yields and turnover rates in photocatalytic hydrogen production systems was Eosin Y, a brominated derivative of the fluorophore fluorescein (Figure 4). In aqueous conditions Eosin Y contains a major absorption peak at 524nm. As UV-visible light emitted by the sun overlaps this region Eosin Y is an ideal candidate for solar driven hydrogen production.^{9, 10} The efficiency of hydrogen evolution systems is often evaluated through the quantum yield, quantum efficiency, and turnover rate of the system. The quantum yield of a photosensitizer is the number of photons emitted per photon absorbed, while the quantum efficiency of photochemical system is the number of electrons excited per

photon absorbed. Both quantum yield and quantum efficiency are reported as ratios from 0-1 or as percentages. The turnover rate is the number of catalytic cycles per photocatalytic system per unit of time. Photocatalytic hydrogen production systems using Eosin Y have had variable success with turnover rates and quantum yields reported up to 900 sec^{-1} and 4% for nonconnected molecular systems.⁹ Unfortunately, Eosin Y exhibits high decomposition and catalysis ceases after extended use in molecular systems limiting its use in larger scale production.^{9,10} Interestingly, recent studies conjugating Eosin Y to graphene and nanotube frameworks have led to a decrease in decomposition suggesting that the degradation process is not innate to Eosin Y.¹¹⁻¹³

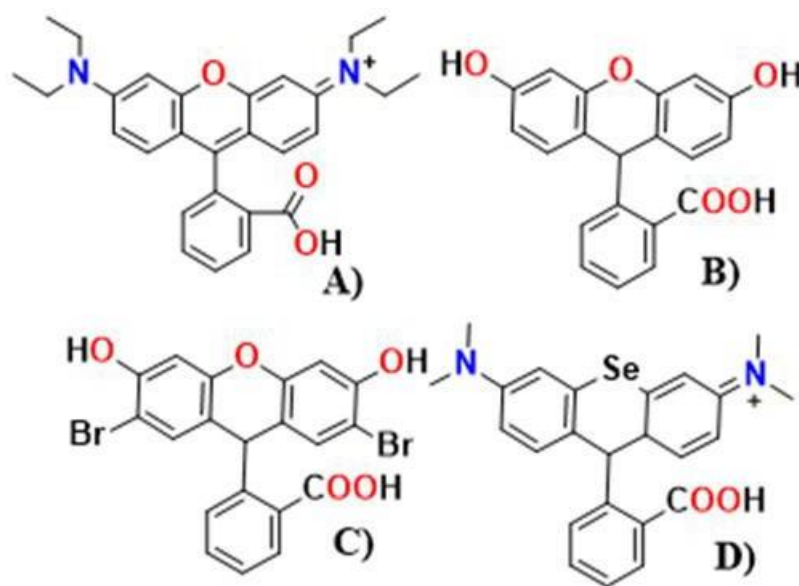


Figure 4. Structures of A) Rhodamine B) Fluorescein C) Eosin Y and D) rhodamine complex in which oxygen is substituted for selenium.

Another derived organic dye that has seen a large amount of use in photocatalytic hydrogen production systems is rhodamine. Historically, rhodamine and its derivatives have been primarily utilized as imaging agents to probe biological systems. One of the most notable uses of rhodamine based dyes are in enzyme linked immunosorbent assays to probe antigen-antibody binding interactions. Similarly to Eosin Y, rhodamine absorbs light in the visible spectrum at around 610

nm.¹⁴⁻¹⁶ One of the more effective molecular hydrogen production systems using a modified rhodamine dye was reported in 2010 by McCormick, *et al.*¹⁷ In this study, a selenium based rhodamine dye was synthesized and placed in solution with a cobaloxime hydrogen evolution catalyst. From this system a turnover rate of $>5,500 \text{ h}^{-1}$ was reported in conjugation with a very high quantum efficiency of 33%. Similarly to the Eosin Y systems, the rhodamine dye suffered from decomposition over extended periods of time.

While dye-sensitized solar cells provide a promising solution for material based photocatalytic hydrogen production systems, in molecular systems they are limited by extensive decomposition. Another approach to photosensitizers in molecular hydrogen production lies in the use of transition metal based complexes. In contrast to the π to π^* transition found on dye sensitizers, the fundamental transition governing a typical transition metal photosensitizer lies in the presence a symmetry allowed metal-ligand charge transfer (MLCT) located in UV-visible region. (Figure 5). This transition allows for excitation of the metals onto the ligand scaffold and subsequent relaxation of electrons onto a linker or hydrogen evolution catalyst.^{18, 19}

Perhaps the most prototypical and ubiquitous transition metal-based photosensitizer utilized in hydrogen production is tris(bipyridine)ruthenium (II) chloride, ($[\text{Ru}(\text{bpy})_3]\text{Cl}_2$). (Figure 6) Along with a π to π^* and d to d transition located in the UV-Visible spectrum, $[\text{Ru}(\text{bpy})_3]\text{Cl}_2$ contains a metal-to ligand charge transfer band at around 452 nm that has a large extinction coefficient ($14,600 \text{ M}^{-1}\text{cm}^{-1}$) along with a surprisingly long lived excited state (650 ns).¹⁹⁻²¹ This long lived excited state and high extinction coefficient has resulted in a myriad of hydrogen evolution systems with large quantum efficiencies and turnover rates containing $[\text{Ru}(\text{bpy})_3]^{2+}$.^{10, 17, 19, 22}

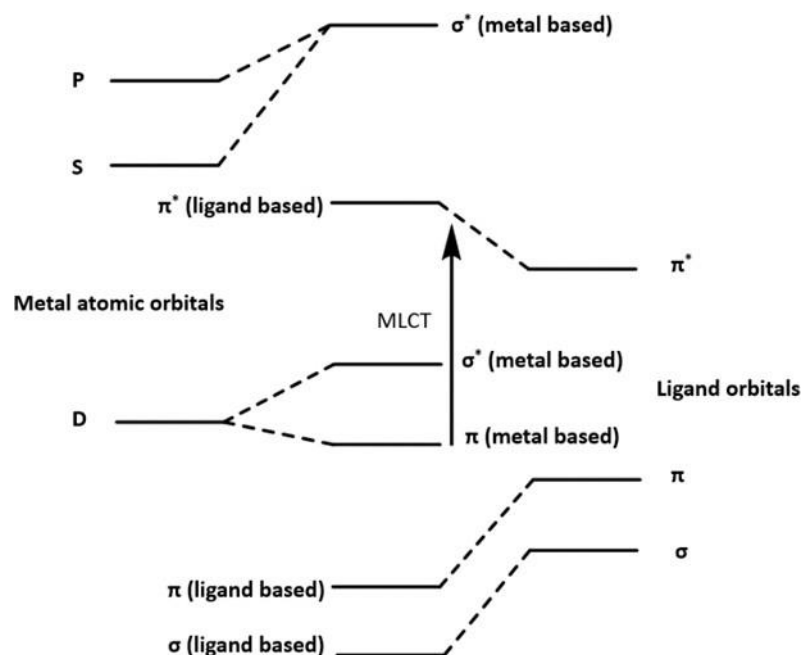


Figure 5. Simplified molecular orbital diagram of a transition metal complex containing a metal ligand charge transition. Adapted from Mauro *et al.* with information from Miessler *et al.*^{18, 23}

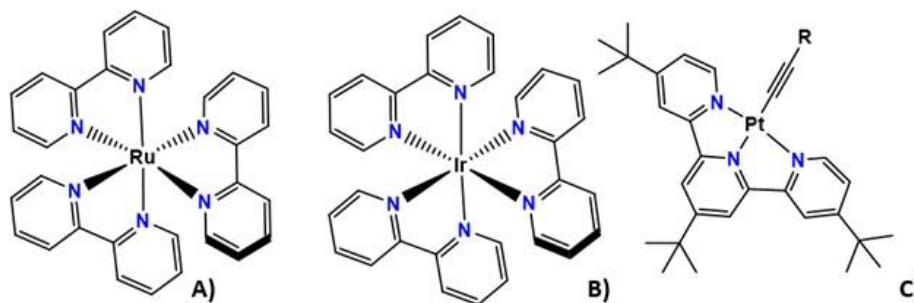


Figure 6. Structures of the photosensitizers A) [Ru(bpy)₃]²⁺, B) [Ir(bpy)₃]³⁺, and C) [Pt(^tBu₃tpy)([C≡CC₆H₄]H)]. In typical systems the para position of one or multiple pyridine ligands are substituted to allow for conjugation or modification of the electronic structure.

Hydrogen Evolution Catalysts

Initial hydrogen evolution catalysts were often discovered serendipitously. From these compounds, redox active molecules were evaluated through kinetic studies of hydrogen production. The catalytic activity of chloro(pyridine)cobaloxime (III) was discovered under such principles (Figure 7). Chloro(pyridine)cobaloxime (III) has served as a benchmark in terms of the stability and rate of hydrogen production in molecular systems for the past several decades. Chloro(pyridine)cobaloxime (III) was first synthesized by Schrauzer, *et al* in 1968 and was further determined to be a highly redox active system.²⁴ Since its characterization a large number of hydrogen evolution systems have utilized chloro(pyridine)cobaloxime (III).^{9, 10, 17, 22} However, as more recent work has shifted to linked systems the use of chloro(pyridine)cobaloxime (III) has decreased as research has indicated high ligand lability when connected in the axial position.¹⁰ The ligand lability issue is resolved with the attachment in the equatorial position at the cost of decreased efficiency due to short excited state lifetimes.²⁵

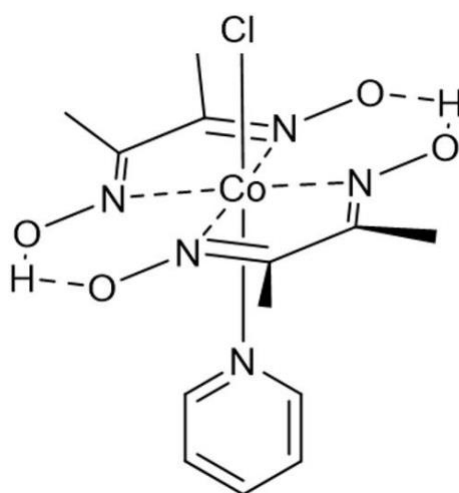


Figure 7. Structure of chloro(pyridine)cobaloxime (III).

More recent hydrogen evolution catalysts have been designed on the basis of mimicking the active sites of natural hydrogenases that catalyze the hydrogen evolution reaction under the premise that nature has optimized the catalytic process. Hydrogenases are large proteins composed of a multitude of subunits and active sites. The active sites of typical hydrogenase are composed of either a single [Fe]-center, a [Fe-Fe]-center, or a [Ni-Fe]-center coordinated by cysteine residues along with low spin ligands such as carbon monoxide and cyanide along with bridging sulfides (Figure 8). While [Fe-Fe]-hydrogenases are notoriously sensitive to the presence of oxygen, [Ni-Fe]-hydrogenases demonstrate increased tolerance to aerobic conditions.²²

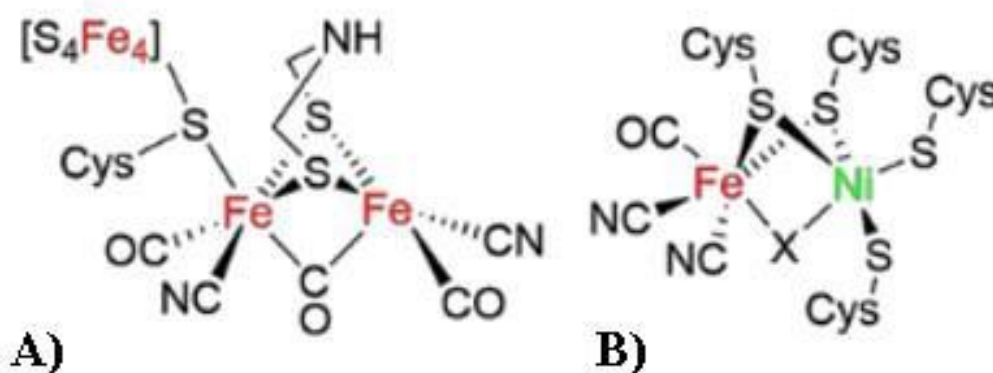


Figure 8. Structures of a (A) typical [Fe-Fe]-hydrogenase active site and (B) a [Ni-Fe]-hydrogenase active site observed in natural hydrogenases.

Work has been done to design and synthesize several molecular variants of the [Fe-Fe] active sites as well as the [Ni-Fe] active sites for use in hydrogen production. One of the first successful biomimetic hydrogen evolution catalysts was synthesized as a variant of a [Fe-Fe] active site by Lyon, *et al* in 1999 (Figure 9).²⁶ Another highly impactful biomimetic hydrogen evolution catalyst were reported by Helm, *et al* in 2012 in the form of a nickel catalyst utilizing multiple phenyl phosphine moieties to imitate the electronic and steric properties of a [Ni-Fe] active site (Figure 8). To date,

this catalyst has demonstrated one of the highest turnover rates by a molecular catalyst at 1040 sec^{-1} with some derivatives reaching $100,000 \text{ sec}^{-1}$.²⁷

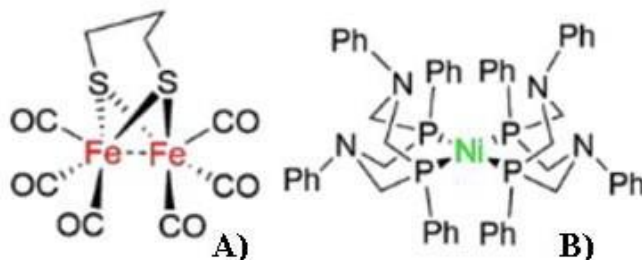


Figure 9. (A) [Fe-Fe] based molecular hydrogen evolution catalysts synthesized by Lyon, *et al* in 1999.²⁶ (B) [Ni-Fe] centered hydrogen evolution catalyst synthesized by Helm, *et al* in 2012.²⁷

While some researchers have found success mimicking the active sites of biological hydrogenases others have taken the approach of creating functional mimics of material and nanoparticle-based hydrogen evolution catalysts. The water gas shift method of producing hydrogen relies on the use of various solid metallic surfaces in a form of heterogeneous catalysis. There are several other catalytic surfaces outside of the water gas shift reaction that have been utilized to promote the hydrogen evolution reaction. One such surface features molybdenum or tungsten disulfides deposited on a layer of silica and has demonstrated significant light driven hydrogen evolution catalysis in conjunction with fluorescein.²⁸ In an effort to reproduce this result on a molecular level, Eckenhoff, *et al* synthesized a series of molecular molybdenum hydrogen evolution catalysts designed to mimic a surface deposit of metal disulfides on silica (Figure 10).²⁹ The most promising of these complexes, $\text{Mo}(\text{bdt})_2(\text{t-BuNC})_2$ yielded a turnover rate of 520 sec^{-1} which falls short of turnover rates reported from biological hydrogenase mimics but provides a promising alternative model for synthesizing new hydrogen evolution catalysts.

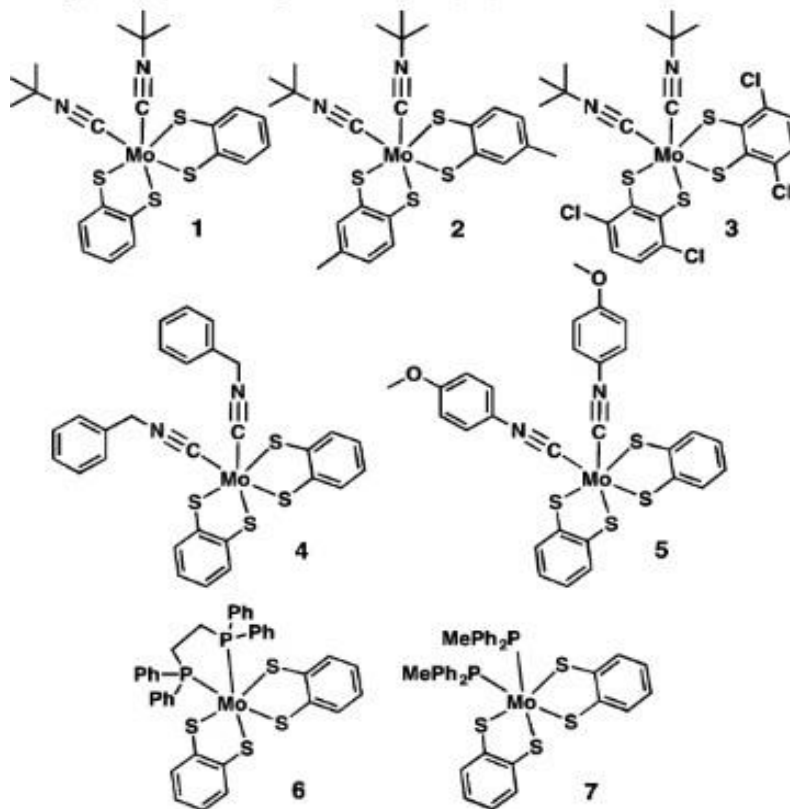


Figure 10. Range of molecular dithiol molybdenum-based hydrogen evolution catalysts synthesized by Eckenhoff *et al* designed to mimic material-based molybdenum catalysts for hydrogen production.²⁹

The catalysts described so far have come about from the applications of redox active systems, biomimicry, and molecularization of material catalysts. In each case, the catalyst was separate from the photoactive molecule. With the purpose of combining the active photosensitizer and hydrogen evolution catalyst Pitman *et al* constructed the iridium catalyst $[\text{Cp}^*\text{Ir}(\text{bpy})(\text{Cl})][\text{Cl}]$ (Figure 11). The premise of the bipyridine and cyclopentadiene ligands being to provide a pi conjugated photoactive system while the five-coordinate iridium center acts as the hydrogen evolution catalyst. The end result was a novel one-component photoelectrocatalyst capable of producing hydrogen gas with a turnover rate of 16.5 sec^{-1} without the use of a secondary photoactive or catalytic complex.³⁰

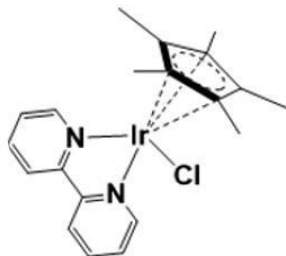


Figure 11. Structure of the Photoelectrocatalyst, $[\text{Cp}^*\text{Ir}(\text{bpy})(\text{Cl})][\text{Cl}]$.

Photocatalytic Hydrogen Production System Linkers

Classical molecular hydrogen production systems are composed of a photosensitizer, a linker, and hydrogen evolution catalyst. In such system a catalysis necessitates a large number of intermolecular collisions, not only between the catalyst and substrate, and also between the catalyst and photosensitizer, as well as the photosensitizer and sacrificial electron donor. In an effort to decrease the number of collisions needed for catalysis and in turn increase catalytic efficiency, researchers began to link the hydrogen evolution catalyst to the photosensitizer. This can be done in several different ways, the simplest of which is a short organic linker or a direct linkage. One of the first directed linkages reported between a hydrogen evolution catalyst and photosensitizer was performed by Fihri, *et al* in 2008 in which a cobaloxime catalyst was linked to a tris(bipyridine)ruthenium (II) photosensitizer building a foundation for connected reactivity with a cobaloxime catalyst.³¹ This work was followed up upon by Mulfort, *et al.* in 2010 and again in 2016 in which the group built several supramolecular assemblies linking a cobaloxime hydrogen evolution catalyst to tris(bipyridine)ruthenium at the axial and equatorial positions and investigated the effect on photoinduced electron transfer (Figure 12).^{25, 32, 33} It was determined that while attachment at the equatorial positioned improved complex stability, however, it also decreased catalytic effectiveness. The catalytic efficiency of supramolecular systems containing

cobaloxime was determined to be limited by ligand lability and electron back transfer; however, these studies provided evidence towards improved catalytic efficiency in connected systems.¹⁰

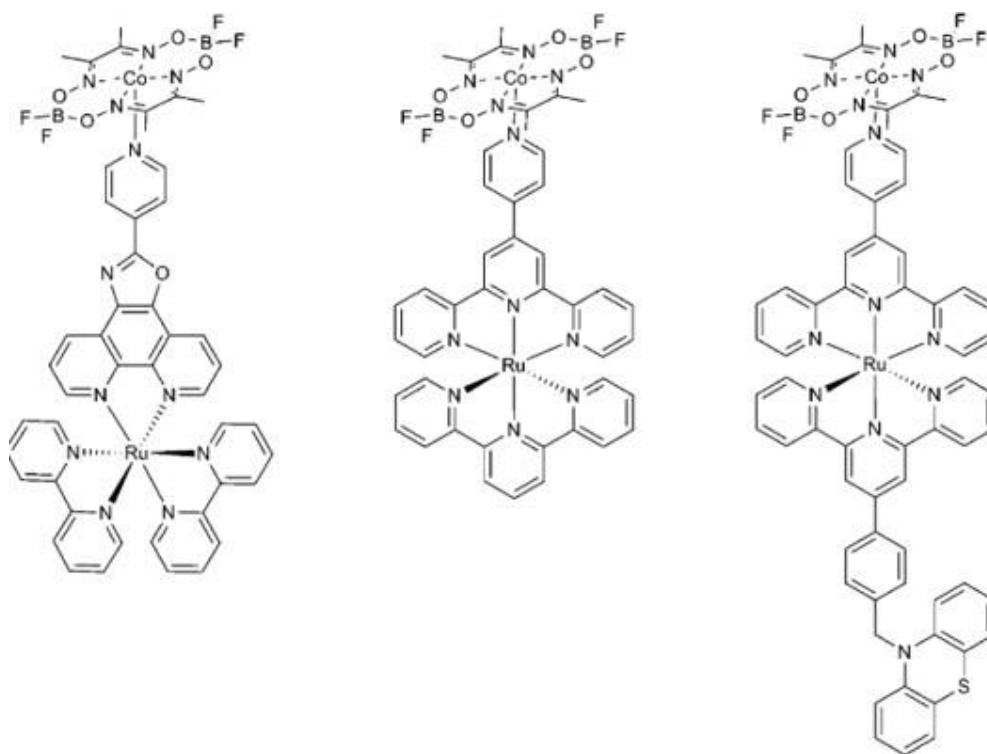


Figure 12. Several of the supramolecular hydrogen production system synthesized by the Mulfort group in 2010.³²

In an effort to move away from direct linkages between components, nanoparticles have also offered a solution towards increasing catalytic rate as a supramolecular system as they have demonstrated the capability to not only prevent back transfer of electrons but to also provide a location for electrons to inhabit prior to proton reduction. Initial interest into nanoparticles as electrostatic linkers focused on a titanium dioxide core structure (Figure 13). However, cadmium selenide, and zinc sulfur cores have also been investigated for their use as linkers in conjunction with cobaloxime catalysts and ruthenium photosensitizers with promising results.^{33, 34}

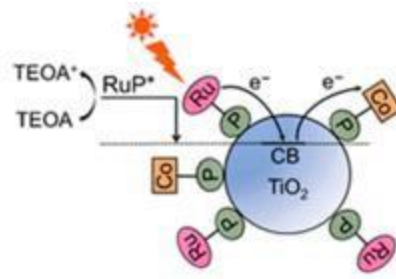


Figure 13. Schematic of a titanium dioxide nanoparticle linking multiple ruthenium-based photosensitizers and cobaloxime hydrogen evolution catalyst utilizing TEOA as a sacrificial electron donor.³¹

Following a similar rationale to nanoparticle-based linkers, researchers have recently become interested in the utilization of protein linkers under the premise that nature has optimized the process of electron transfer over the course of millions of years. Furthermore, proteins can be easily altered through modern day mutagenesis techniques such as site-directed mutagenesis or CRISPR to allow for optimization of system connectivity and to tune the electron transfer pathway. One of the highest rates of hydrogen production was reported by Kandemir *et al* in 2016, in which a cobalt catalyst attached to a cytochrome c protein provided a turnover of rates of $>250,000 \text{ h}^{-1}$.³⁵ Unfortunately, these large turnover numbers required the use of electrocatalytic, rather than photocatalytic conditions, and similar results have not been reported to date for any photocatalytic system.

Outside of electrocatalytic conditions, researchers have used small electron transfer proteins such as flavodoxins and ferredoxins to achieve turnover rates up to 650 h^{-1} (Figure 14).^{22, 37, 38} Similarly, artificial peptide sequences have also been investigated with lower levels of success,^{39, 40} likely due to the fact that these peptides do not provide a binding pocket to stabilize the catalyst within the protein environment.²² While small electron transfer proteins have been proved to be relatively effective linkers in hydrogen evolution systems, the highest photocatalytic turnover rates have

been achieved when using larger charge transfer proteins such as photosystem I (PSI), which have multiple photoreceptors and elaborately designed electron-transfer pathways.

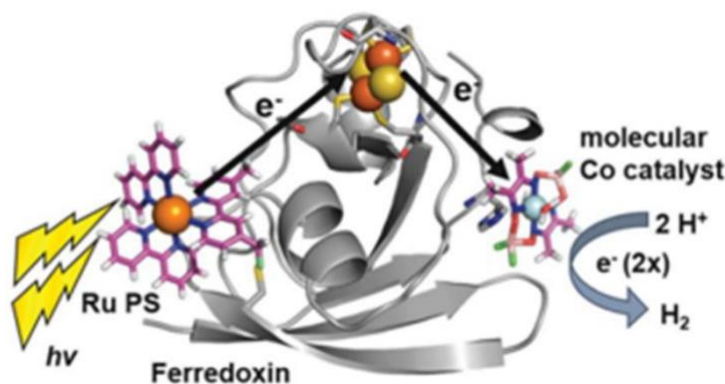


Figure 14. Protein based photocatalytic hydrogen production system in which ferredoxin is used to link a molecular cobaloxime hydrogen evolution catalyst to tris(bipyridine)ruthenium (II).³⁷

Another approach to utilizing proteins as a form of linker in a photocatalytic hydrogen production system is to use a protein that is photochemically active. Naturally, photosystem I (PSI) has become a popular photoactive protein for use in such systems as nature has optimized PSI to become a natural solar panel, using chlorophyll molecules with the ability to absorb visible light and transfer it to the primary electron donor, P700, with large amounts of electrical potential.⁴¹ Utschig, *et al*, in a series of papers, demonstrates that multiple catalytic units of molecular cobaloxime or nickel diphosphine catalysts molecules could be connected to PSI through electrostatic and hydrophobic interactions to create a large macromolecular hydrogen production system.^{5, 42, 43} Through the use of such a system PSI was capable of acting as a large electron shuttle providing electrons to a number of attached catalytic subunits. The most efficient molecular catalyst system, a cobaloxime-PSI hybrid, yielded a turnover rate of 2.83 sec⁻¹ that persisted over a period of 1.5 hours before loss of the Co catalyst giving rise the hypothesis that covalent

attachment of the catalyst may extend catalytic lifetime. The advantages of these systems are highly apparent, but protein-catalyst degradation is still a major issue to overcome.

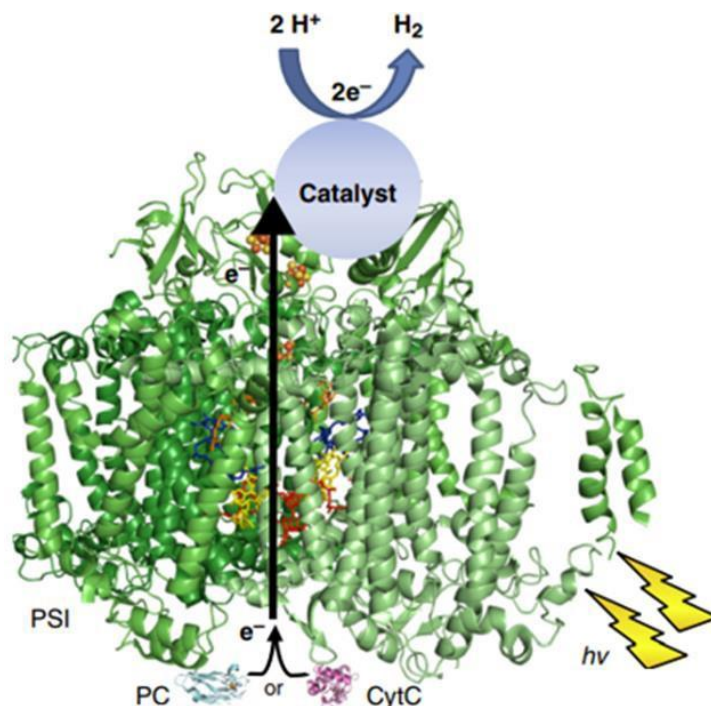


Figure 15. PSI-based photocatalytic hydrogen production system in which a hydrogen evolution catalyst is attached the PSI system that acts as a photosensitizer.^{5, 42, 43}

Synthesis of a $[\text{Cp}^*\text{Ir}(\text{bpy})(\text{Cl})][\text{Cl}]$ -Rubredoxin Hydrogen Evolution System.

The aim of this thesis is to synthesize and characterize a hydrogen evolution system utilizing a $[\text{Cp}^*\text{Ir}(\text{bpy})(\text{Cl})][\text{Cl}]$ photoelectrocatalyst in conjunction with a rubredoxin protein. Rubredoxins are small electron transfer protein (5-6 kDa) found in sulfur metabolizing bacteria. They have similar properties to ferredoxins except instead of a $[2\text{Fe}-2\text{S}]$ centers with two iron atoms coordinated by bridging sulfides and four cysteine protein ligands they contain a single Fe center coordinated by four cysteine residues. Rubredoxins are thermodynamically and kinetically stable in an aerobic aqueous environment.⁴⁴⁻⁴⁶ Recent work has demonstrated that rubredoxins are capable of acting as a hydrogen evolution catalyst in solution with the substitution of the iron

center for nickel.⁴⁷ Work with ferredoxins and flavodoxins as electron transfer linkers has not yet shown any ability to directly substitute the coenzymes for another redox active metal for hydrogen production. Flavodoxins that do not contain a natural internal metal center, but contain a flavin mononucleotide (FMN) cofactor. Ferredoxins, with an [2Fe-2S] cluster, can catalyze the hydrogen evolution reaction when linked to a hydrogen evolution catalyst and photosensitizer.^{38, 48} As such, the premise of this work is that the novel [Cp*Ir(bpy)(Cl)][Cl] will act as both a photosensitizer and a hydrogen evolution catalyst while rubredoxin acts as a location for electron localization and electron collection during the hydrogen evolution reaction.

To provide supporting evidence for this work, rubredoxin will first be connected to the hydrogen evolution catalyst chloro(pyridine)cobaloxime(II) as well as a modified version of the photosensitizer tris(bipyridine)ruthenium(II). Mutations will be made to allow for the presence of a single cysteine and histidine residue around 12-15 Å from the Fe center. Attachment of chloro(pyridine)cobaloxime will take place through the substitution of the axial pyridine ligand in exchange for the imidazole of the histidine. The photosensitizer will then be attached to the cysteine residue through the nuclear substitution of a bromine built into the bipyridine ligand by the thiol of the cysteine. This classical method of protein based photocatalytic hydrogen production will serve as a basis for changes in efficiency in the [Cp*Ir(bpy)(Cl)][Cl]-Rubredoxin system in which [Cp*Ir(bpy)(Cl)][Cl] will replace the photosensitizer.

Methods

Expression and Mutagenesis

Digestion of vectors

The wild type DNA sequence for rubredoxin was procured from Invitrogen. To express rubredoxin the sequence had to be located inside a vector containing a promoting region. The pME-T vector the rubredoxin gene was received in did not contain such a region. To fix this issue, the received plasmid along with an empty pET21a(+)-HpDsbG vector (obtained from Addgene, plasmid # 39329) were digested using the two restriction enzymes *XhoI* and *NdeI* following a standard protocol for restriction enzyme digests outlined by New England Bio-Labs.

The received plasmid was dissolved in 50 μ L of deionized water and mixed by flicking and centrifuging. Two reaction solutions consisting of the reagents shown in Table 1 were prepared for both the pEM-T vector containing the rubredoxin gene and the empty pET21a(+)-HpDsbG (pET21a) vector.

Table 1. Table illustrating the volume of each reagent used in both the pEM-T digest reaction and the PET21a digest reaction.

Reagent	pEMT-T Reaction	Pet21a Reaction
Vector	10uL	28.57uL
<i>NDE I</i>	1uL	2uL
<i>XHO I</i>	1uL	2uL
Cutsmart Buffer	2uL	4uL
Deionized Water	6uL	43uL

The reaction solutions were incubated at 37 °C for one hour. After incubation, the reaction solutions were loaded into a gel for electrophoresis resulting in several distinct DNA bands as

shown in Figures 21 and 22. After the digestion, the DNA was purified using a S.N.A.P Gel Purification kit combined with a standard protocol both purchased from Invitrogen.

The two gel pieces containing the desired DNA were cut out using a clean razor. The resulting pieces were estimated to be around 100 μ L and were transferred to sterile 1.5 mL microcentrifuge tubes. 250 μ L of 6.6 M sodium iodide were added to both microcentrifuge tubes and the resulting solutions were incubated in a 45°C water bath until melted, at which point they were returned to room temperature. 525 μ L of binding buffer was added to both microcentrifuge tubes and mixed with gentle inversion. A S.N.A.P purification column was assembled following the instructions detailed in the Gel Purification Kit and the contents of the microcentrifuge tubes were loaded onto them. The columns were centrifuged into microcentrifuge tubes for 30 seconds at 10,000 rpm and the liquid was loaded back onto the columns, the process of centrifugation and loading was repeated twice more. The columns were then placed into two new microcentrifuge tubes and 40 μ L of nuclease free sterile water was added to the column. After which they were then centrifuged at 10,000 rpm for 2 minutes to elute the DNA into the microcentrifuge tube which was subsequently placed on ice. To determine the purity and concentration of DNA for use in future steps the Beer-Lambert Law was used in conjunction with UV-Visible spectroscopy. The Beer-Lambert Law relates absorbance of a solution to the concentration of a solution in the following equation:

$$A = \epsilon bc \quad (\text{equation 1}).$$

A being absorbance, ϵ being the molar absorptivity, b being path length, and C being concentration. UV-visible spectroscopy measurements on protein samples were carried out by measuring the sample's absorbance as a function of wavelength of light using a quartz cuvette

containing a 1 cm path length. While pure DNA shows a maximum absorbance at 260 nm, protein shows maximum absorbance at 280 nm. Using this method and understanding that the molar absorptivity of double stranded DNA is 50 $\mu\text{g}/\text{mL}$ the concentration of DNA was determined.⁴⁹

Along with determining a concentration, UV-Vis spectroscopy can give an estimation to the purity of a sample by comparing the ratio of DNA to protein present in a sample. The amount of protein present in the sample was determined by measuring the absorbance of light at 280nm. Along with determining a concentration, UV-Vis spectroscopy can be used to estimate the purity of a sample by comparing the ratio of DNA to protein present in a sample.

Ligation of gene insert and vector backbone

After both the pET21a(+)HpDsbG vector backbone and rubredoxin gene insert were retrieved and their concentration and purity determined both the vector and insert were ligated together using an instant ligation master mix obtained from New England BioLabs along with the associated protocol.

The ligation reaction consisted of 0.91 μL of 1:10 diluted rubredoxin insert along with 2 μL of the cut pET21a(+)HpDsbG vector bringing the molar ratio of vector to insert to 1:3. The volume of the solution was brought up to 5 μL through the addition of nuclease free water and 5 μL of the ligation master mix was added. The final solution was mixed by pipetting up and down 10 times. 2 μL of the reaction solution was added to a 50 μL aliquot of DH5 α competent cells designed for optimal transformation efficiency and placed on ice for 30 minutes. The cells were then heat shocked at 42°C for 30 seconds and returned to ice for two minutes to induce transformation. 950 μL of LBA media was added to the microcentrifuge tube and the solution was incubated one hour with shaking at 37°C. After shaking, 100 μL of the solution was spread on LBA plates and left to incubate overnight at 37°C to promote colony growth. The following afternoon, a single colony

was placed inside a 10 mL solution of LBA media to initiate the creation of a starter culture. The media solution was left overnight at 37°C with shaking stimulating cell growth.

The DNA was purified by extracting the previous night's cell culture using an Illustra plasmid prep mini spin kit bought from the GE Healthcare along with the following procedure supplied by GE Healthcare.

The cell culture was centrifuged at max speed for 10 minutes and excess supernatant was removed leaving behind a pellet of cells. The cell pellet was re-suspended in 175 µL of lysis buffer type 7 to begin the process of destroying the cell membranes. After resuspension, the solution was transferred to a microcentrifuge tube and treated with 175 µL of lysis buffer type 8 and mixed with gentle inversion until the solution became clear with a white precipitate. 350 µL of lysis buffer type 9 was added to neutralize the lysis buffer type 8 and immediately mixed by gentle inversion until the white precipitate was evenly dispersed. The microcentrifuge tube containing the solution was centrifuged at max speed to isolate the precipitate at the bottom. The cell lysate was removed by pipetting carefully around the white precipitate, loaded onto a wash column, and centrifuged at max speed for 30 seconds. After centrifugation, the column was washed with 400 µL of wash buffer type 9 and centrifuged for 30 seconds at full speed. After washing the column with wash buffer type 9 and centrifuging, 400 µL of wash buffer type 1 was loaded onto the column and the column was centrifuged again at max speed. To elute the DNA, 100 µL of elution buffer type 4 was loaded onto the column and left to incubate for 30 seconds. After incubation, the column was centrifuged one last time at max speed and the flow thru was collected in a new sterile microcentrifuge tube. The DNA concentration and purity was then determined using UV-visible spectroscopy by evaluating the concentration of protein (280 nm) and comparing it to the concentration of DNA (260nm).

Transformation of rubredoxin plasmid into BL21 competent cells

The DH5 α cell line was designed with DNA replication in mind. In order to express the wildtype rubredoxin protein, the plasmid was transferred to BL21 competent cells which have been optimized for expression of protein. This was done using the following protocol.

1.2 μ L (100ng) of the reaction solution was added to a 50 μ L aliquot of BL21 competent cells designed for optimal expression efficiency and left to sit on ice for 30 minutes. The cells were then heat shocked at 42°C for 30 seconds and returned to ice for two minutes to initiate the transformation process. 950 μ L of LBA media was added to the microcentrifuge tube and the solution was incubated one hour with shaking at 37°C. After shaking, 100 μ L of the solution was spread on LBA plates and left to incubate overnight at 37°C to promote colony growth. The following afternoon, a colony was placed inside a 10 mL solution of LBA media to create a starter culture. The media solution was left overnight at 37°C with shaking stimulating cell growth.

Expression and purification of the wild-type Rubredoxin protein.

To prepare for the expression of the wild type protein, a 1 L solution of LB media containing 0.4% glycerol and 0.1 M ferric chloride was prepared. One starter culture was poured into the LB media and the entire solution was incubated at 37°C with shaking. The optical density of the solution was monitored via UV-Visible spectroscopy until the solution reached an optical density of 0.86. At this point 1 mM isopropyl β -D-1-thiogalactopyranoside (IPTG) was added to the solution to induce expression of the rubredoxin gene. The solution was subsequently left to incubate overnight at 18°C with shaking.

The following day the solution was centrifuged at 6900 g for 10 minutes. The supernatant was pipetted out of the tube and the mass of the cell pellet was determined. The cells were then re-suspended in a 50 mM solution of Tris-HCl pH 8.0. A cell lysate solution was prepared by adding

phenylmethylsulfonyl fluoride (PMSF) to the resuspended pellet to create a 1 mM solution, after which egg white lysozyme was added to the solution to create a final concentration of 0.3 mg/ml. Further cell lysis was induced by sonicating the cell extract with six 30 second cycles of ultrasonic pulses followed by 5-minute cooling cycles on ice.

To prepare for purification a column containing a nickel-NTA resin was equilibrated with a solution containing a 20 mM potassium phosphate, 10 mM imidazole, and 10% glycerol at a pH of 8.0. The cell lysate was slowly loaded onto the column followed by a wash buffer containing a solution of 20 mM potassium phosphate, 25 mM imidazole and 10% glycerol, pH 8.0. After the wash buffer drained through an elution solution containing 20 mM potassium phosphate, 250 mM imidazole, and 10% glycerol, pH 8.0 was washed through the column. Fractions were collected throughout this process.

To concentrate the rubredoxin protein, 4 mL of fractions containing the rubredoxin, collected during the elution step were placed into molecular weight filters with a 3000 Da cutoff. The filters were centrifuged at 4,000 rpm for 20 minutes. This process was repeated until the fractions were completely concentrated. To estimate the concentration of the protein sample a Bradford assay was used¹⁶. A Bradford assay is performed by incubating protein samples with a colorimetric dye reagent and measuring the absorbance of the dye-protein adduct at 595 nm. The dye absorbance is proportional to the amount of protein present in solution. By knowing the protein concentration associated with each absorbance, an unknown concentration of a protein can be determined.

The first step of running a Bradford assay is to create a standard curve. This was done by combining 800 μ L of varying concentrations of bovine serum albumin with 200 μ L of Bradford assay dye, incubating 10 minutes at room temperature, and measuring the absorbance at 595 nm with UV-Vis spectroscopy. The concentrations of bovine serum albumin used were 2 μ g/mL, 4

$\mu\text{g/mL}$, $6 \mu\text{g/mL}$, $8 \mu\text{g/mL}$, and $10 \mu\text{g/mL}$. Using Microsoft Excel, the concentration of protein to absorbance was plotted and a standard curve was obtained. After a standard curve was obtained, concentrated rubredoxin protein was diluted 1:50 and $800 \mu\text{L}$ of the diluted protein was added to $200 \mu\text{L}$ of dye. The final solution was incubated for 10 minutes at room temperature and the absorbance was measured at 595 nm using UV-Vis spectroscopy. This dilution was necessary to produce a solution a solution with an absorbance within the range of the standard curve. Using the standard curve, the concentration of rubredoxin was estimated in mg/mL .

To determine the purity of the rubredoxin protein sodium dodecyl sulfate (SDS) polyacrylamide gel electrophoresis was performed. The samples included the wash, flow, supernatant, pellet, and elution fractions. $50 \mu\text{L}$ of each sample was added to $50 \mu\text{L}$ of 2x SDS dye. Samples were heated at 85°C for 10 minutes before being loaded onto the gel. The gel was run until the tracking dye was present at the bottom of the gel. Once finished, the gel was placed into a plastic container containing Coomassie stain and incubated for one hour with shaking. The liquid was subsequently drained off and the gel was exposed to a destaining solution containing 45% methanol, 45% water and 10% acetic acid in order to remove excess dye. A picture was then taken of the gel with a Pharos FX molecular imager (Bio-Rad).

Mutagenesis of the wild type Rubredoxin DNA

In order to successfully connect the modified tris(bipyridine)ruthenium photosensitizer and the catalyst chloro(pyridine)cobaloxime to the protein rubredoxin, two mutations must be introduced to the rubredoxin protein. First the serine at position 22 must be changed to a cysteine and second, the aspartic acid at position 35 must be changed to a histidine. To make these two mutations the following primers (Figure 16) containing the desired mutation were ordered from Invitrogen.

Aspartic Acid to Histidine: Changing 159G to 159C

Sequence:

5' TTTGAAGATCTGCCG**CAT**GATTGGGCATGTCCG3'

3' AAACCTTCTAGACGGC**GTA**CTAACCCGTACAGGC5'

Primers

5' TTTGAAGATCTGCCG**CAT**GATTGGGCATGTCCG 3' Tm:77°C: 52% GC 33bp in length:
Anneal at 72°C (Calculated Tm 79°C)

3' AAACCTTCTAGACGGC**GTA**CTAACCCGTACAGGC 5' Tm:75°C: 52% GC 33bp in length:
Anneal at 72°C (Calculated Tm 79°C)

Serine to Cysteine: changing 159G to 159C

Sequence:

5' GCAAAAGGTGATCCGGAT**TGCG**GTATTAAACCGGGTACAAAATTT3'

3' CGTTTTCCACTAGGCCTA**ACG**CCATAATTTGGCCCATGTTTTAAA5'

Primers

5' GCAAAAGGTGATCCGGAT**TGCG**GTATTAAACCGGG3' Tm:77°C: 51% GC 35bp in length:
Anneal 72°C (Calculated Tm 80°C)

3' CGTTTTCCACTAGGCCTA**ACG**CCATAATTTGGCCC5' Tm:77°C: 51% GC 35bp in length:
Anneal 72°C (Calculated Tm 80°C)

Figure 16. Primers utilized to generate rubredoxin mutations.

A Quik-Change II site directed mutagenesis kit was obtained from Agilent Technologies containing a protocol along with reagents. Reactions containing the reagents and volumes illustrated in Table 3 were set up inside PCR tubes. The solutions tubes containing the reactions were placed inside a thermal cycler and the protocol outlined in Table 4 was followed.

Table 3. Illustration of the reagents and volumes used for the mutagenesis reaction.

Reagent	Control Reaction	S22C	D35H
Reaction Buffer	5uL	5uL	5uL
Control Plasmid	2uL	1uL	1uL
Forward Primer	1.25uL	1uL	1uL
Reverse Primer	1.25uL	1uL	1uL
DNTP Mix	1uL	1uL	1uL
DI water	38.5uL	40.5uL	40uL
DNA Polymerase	1uL	1uL	1uL

Table 4. Outline of the thermal cycler protocol followed during the PCR step of site directed mutagenesis.

Segment	Cycles	Temperature	Time
1	1	95°C	30 seconds
2	18	95°C	30 seconds
		55°C	1 minute
		68°C	5 minutes 30 seconds

After thermal cycling was completed the reactions were placed on ice for 10 minutes. 1 μ L of the *DpnI* restriction enzyme was then added to each reaction in order to digest the parental DNA. The reactions were mixed via pipetting and incubated at 37°C for 1 hour. After digestion, 1 μ L of each reaction along with a control DNA sample was added to 50 μ L of XL1-Blue super competent cells inside of a 14 mL Falcon polypropylene round bottom tube and placed on ice for 30 minutes. The reactions and control were then heat shocked at 42°C for 45 seconds and placed back on ice for 2 minutes. 0.5 mL of NYZ+ broth preheated to 42°C was added to each solution and incubated at 37°C with shaking for 1 hour. The solutions were then plated on LBA plates and left to incubate overnight at 37°C.

Synthesis of modified tris(bipyridine)ruthenium photosensitizer

In order to connect the photosensitizer tris(bipyridine)ruthenium (Fig. 2) to the protein rubredoxin a derivative of the compound containing a bromine, [Ru(4-CH₂Br-4'-(2,2'-bipyridine) (2,2'-bipyridine)₂](PF₆)₂, must be synthesized (Figure. 17).

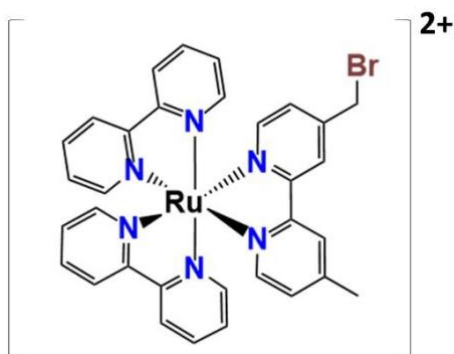


Figure 17. Representation of the bromine derivative of the photosensitizer [Ru(4-CH₂Br-4'-(2,2'-bipyridine) (2,2'-bipyridine)₂](PF₆)₂

4-(bromomethyl)-4'-methyl-2,2'-bipyridine

The synthesis consisted of two separate steps. First, the ligand 4-(bromomethyl)-4'-methyl-2,2'-bipyridine was synthesized through the reaction presented in figure 21. As previously reported in the literature, 1.8 grams of 4,4'-dimethyl-2,2'-bipyridine, 1.8 grams of N-bromosuccinimide and 0.05 grams of isobutyronitrile were added to a 25 mL round bottom flask and dissolved in 40 mL of carbon tetrachloride.²¹ The resulting solution was heated in a nitrogen atmosphere under reflux at 76°C for 2 hours. The reaction was then cooled to room temperature, filtered with a Hersh funnel, and evaporated until dry in an oven. The following day the dried product was dissolved in methylene chloride, loaded onto a silica column, and eluted with a solution of 98:2 (v/v) methylene chloride/acetone. The fractions obtained from the silica column were rotary vaporized to remove

the solvent to obtain a final yield of 33%. A ^1H -NMR spectrum, a ^{13}C -NMR spectrum, and an IR spectrum were obtained for characterizing the final product. To better understand the IR spectra, optimization of the structure and frequency analysis of active IR vibrations was performed under the premise of a simple harmonic oscillator using B3LYP with the G36* basis set in Gaussian09. (Yield: 33%) ^1H NMR (500MHz, CDCl_3 δ): 2.15 (s, 3 H) 4.47 (s, 2 H), 7.35 (unresolved, 2 H), 8.65 (unresolved, 2 H). ^{13}C NMR (500MHz, CDCl_3 δ): 20.0, 30.1, 76.5, 119.1, 122.2, 123.4, 124.1, 125.5, 146.5, 149.8. IR(cm^{-1}): 990 (m), 910 (m), 840 (m), 829 (s), 730 (w), 688 (w), 668 (m), 640 (s), 684 (m), 581 (s), 524 (w).

[Ru(4-CH₂Br-4'-(2,2'-bipyridine)(2,2'-bipyridine)₂](PF₆)₂

After brominating the ligand, 200 mg of $\text{Ru}(\text{bpy})_2\text{Cl}_2$ was placed inside a round bottom flask along with 200 mg of silver triflate. The two compounds were then dissolved in 65 mL of anhydrous acetone and left to stir for 8 hours under nitrogen atmosphere. Over time, a precipitate formed which was filtered out. 100 mg of 4-(bromomethyl)-4'-methyl-2,2'-bipyridine was then added and the solution was stirred for another 2 hours after which the product was precipitated out with the use of concentrated ammonium hexafluorophosphate. The resulting precipitate was filtered and left to dry in an oven overnight. A ^1H -NMR spectrum and UV-visible spectrum of the resulting compound were then obtained. (Yield: 13%) ^1H NMR (500 MHz, CDCl_3 δ): 3.25 (s, 5 H), 7.24 (s, 1 H), 7.45 (s, 1 H), 7.68 (s, 1 H), 8.12 (s, 1 H), 8.78 (s, 1 H), 8.65 (s, 1 H). UV/Visible (H_2O ; λ_{max} , nm): 460, 425, 285, 240.

*Synthesis of [Cp*Ir(bpy)(Cl)]Cl*

Following a similarly reported reaction, 11 mg of the previously synthesized ligand 4-(bromomethyl)-4'-methyl-2,2'-bipyridine and 20 mg of dichloro-(pentamethylcyclopentadienyl)-iridium (III) was dissolved in 3 mL of dichloromethane and left to stir for 15 minutes.²⁸ The

solvent was then evaporated to dryness to obtain a crude yield of 97%. A $^1\text{H-NMR}$ spectrum and UV-visible spectrum was then obtained. The remaining solid was dissolved in a minimal amount of DCM and hexanes were added dropwise until the precipitation of a minimal amount of yellow powder. The powder was dried on the Schlenk line and crystalized via vapor diffusion of diethyl ether on acetonitrile. X-ray crystallographic data was obtained from the crystal. Yield: 13% $^1\text{H NMR}$ (500 MHz, CDCl_3 δ): 1.70 (s, undefined), 4.75 (s, 2 H), 5.00 (s, 2 H), 5.29 (s, undefined), 7.23 (s, 1 undefined), 7.50 (s, 3 H), 7.61 (s, 1 H), 7.63 (s. 1 H), 7.65 (s, 1 H), 7.99 (s, 1 H), 8.62 (s, 3 H), 8.75 (m, unresolved), 8.85 (s, 1 H), 8.98 (s, 1 H), 9.10 (s, 1 H), 9.23 (s, 1 H). UV/Visible (H_2O ; λ_{max} , nm): 420, 390

Initial GC-TCD Experimentation

A standard sample was created by bubbling 3% hydrogen / 97% nitrogen gas into a 5 mL sealed cuvette. To provide a baseline for future hydrogen production, a reaction was set up with 8.9 mM of brominated tris(bipyridine)ruthenium, 7.8 mM chloro(pyridine)cobaloxime and 81 mM ascorbic acid in a total volume of 3.5 mL at a pH of 7.0. The reaction was charged with a stir bar and illuminated with electromagnetic radiation at a wavelength of 455 nm with an LED (ThorLabs) for 24 hours.

An Agilent 7820A GC-TCD was outfitted with a 10 meter in length, 0.32 μm diameter molecular sieve column with a film thickness of 30 μL and heated to 300°C. Samples were injected into the GC at 70°C and passed through the column with a nitrogen carrier flow rate of 5 mL/min prior to being detected by a negative polarity TCD. A standard curve was created by injecting 50 uL, 40 uL, 30 uL, 20 uL and 10 uL of the headspace located on the standard sample utilizing a sealed syringe. One hundred microliters from the headspace of the chloro(pyridine)cobaloxime and

tris(bipyridine)ruthenium reaction was then injected into the GC and the reaction efficiency was evaluated.

Results

Digestion of vectors

Digestion and electrophoresis of the empty pET21a(+)-HpDsbG vector and rubredoxin containing pEM-T vector resulted in the two electrophoresis gels visualized in Figure 18. UV-visible spectroscopy revealed that the concentration of the pET21a(+)-HpDsbG vector following gel purification was 25 $\mu\text{g/mL}$ with a 260 nm/280 nm ratio of 1.35. UV-Vis spectroscopy also determined the concentration of the rubredoxin insert following gel purification to be 45 $\mu\text{g/mL}$ with a 260 nm/280 nm ratio of 1.5.

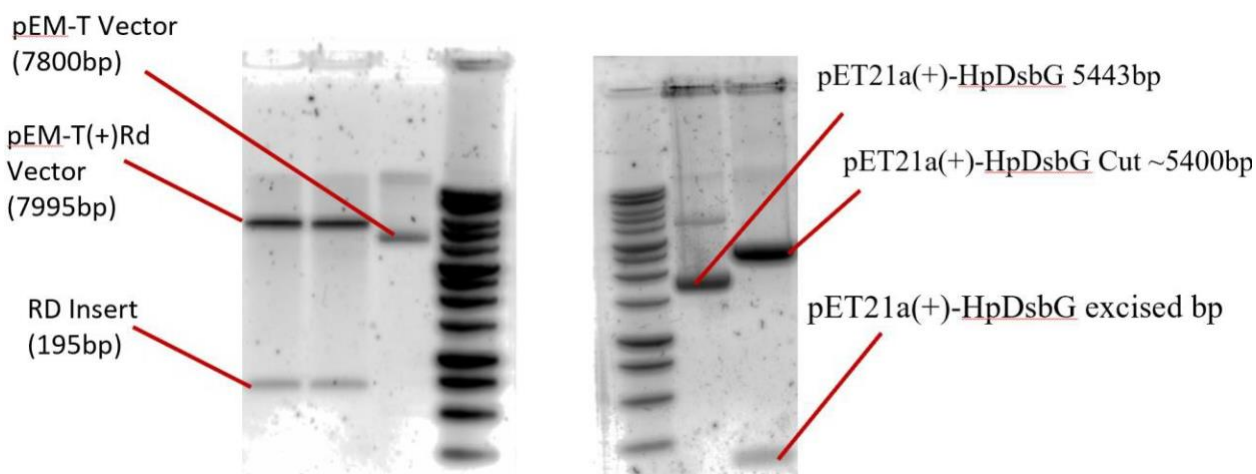


Figure 18. Visualization of the two restriction enzyme digestion reactions. On the left, the digestion of the pEM-T vector is pictured loaded with the following lanes. Lane one and two contain the cut vector, three contains the uncut vector and four contains the ladder. On the right, the digestion of the pET21a(+)-HpDsbG vector is pictured with lane one containing a ladder, two containing the uncut vector, and three containing the cut vector.

Ligation of gene insert and vector backbone

Ligation and electrophoresis of the rubredoxin insert and cut pET21a(+)-HpDsbG backbone resulted in the electrophoresis gel pictured in Figure 19.

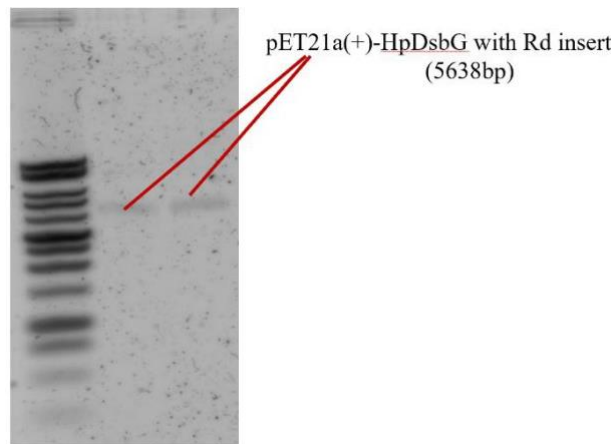


Figure 19. Gel formed from the electrophoresis of the ligated pET21a(+)-HpDsbG backbone and rubredoxin insert. Lane one contains the ladder while lanes two and three contain the ligated plasmid.

UV-Vis spectroscopy determined that the concentration of the ligated vector backbone and rubredoxin insert was 72.5 $\mu\text{g}/\text{mL}$ with a 260 nm/280 nm absorbance ratio of 1.16. Transformation of the ligated plasmid into BL21 competent cells onto LBA plates resulted in several small sized colonies which successfully created four 10 mL cell cultures after growing overnight.

Expression and purification of the wild-type Rubredoxin protein

Once one of the 10 mL starter cultures containing the ligated vector backbone and rubredoxin insert was placed inside of a 1 L flask of enriched LBA media and incubated until the optical density reached 0.859 after 2 hours and 18 minutes. The cells were induced with IPTG to a final concentration of 1 mM and allowed to incubate with shaking for 18 hours. The cells were harvested by centrifugation and following spin down, the resulting cell pellet obtained was 11.35 grams. The procedure listed above in the methods section was followed for the cell lysis and purification on a Ni-NTA column. After chromatography seven fractions were obtained, including

five clear elution fractions. The color of the elution fractions became yellow as they were concentrated.

The use of a Bradford assay determined the resulting protein concentration to be 55.58 mg/mL. Polyacrylamide gel electrophoresis and visualization gave the following gel pictured in Figure 23.



Figure 20. Polyacrylamide gel electrophoresis image of various fractions obtained during the purification of the rubredoxin protein. The lanes are as follows; lane one wash, lane two flow thru, lane three supernatant, lane four pellet, lanes five through nine elution, and lane 10 the standard.

Mutagenesis of the wild type Rubredoxin DNA

Following site-directed mutagenesis of the rubredoxin plasmid as described in the methods section above, colonies were visible on both the standard transformation control as well as the standard mutagenesis control. However, no colonies were visible on the serine to cysteine mutation reaction or the aspartic acid to histidine mutation reaction. Further work to optimize the mutagenesis reactions was unsuccessful.

Synthesis of 4-(bromomethyl)-4'-methyl-2,2'-bipyridine

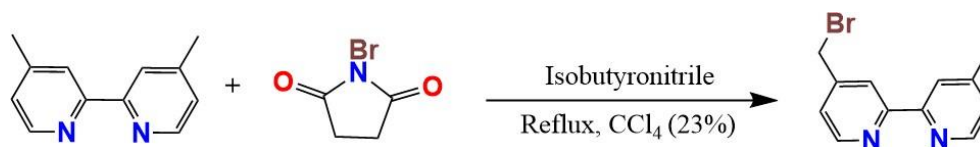


Figure 21. Overall synthesis of modified bipyridine ligand.

The reaction of 4,4'-dimethyl-2,2'-bipyridine with *N*-bromosuccinimide resulted in the filtering of a red-orange chunky powder. Purification of this powder resulted in the collection of several fractions containing an orange tint. Rotary vaporization of these fractions resulted in the formation of the oily white gum pictured in Figure 22 with a 33% yield. The use of ¹H-NMR and ¹³C-NMR spectroscopy on this product produced the spectra shown in Figure 23 and 24 while IR analysis of a KBr pellet yielded the spectrum presented in Figure 25. Finally, geometry optimization and IR frequency calculations of 4-(Bromomethyl)-4'-methyl-2,2'-bipyridine were successful using G36* basis set at B3LYP level. Using the visualization program Avogadro, bands at 678.47 cm⁻¹, 690.22 cm⁻¹ and 754.29 cm⁻¹ were assigned to bending modes in pyridine. On the other hand, band at 569.50 cm⁻¹ corresponded to C – Br stretching.⁵⁰



Figure 22. Oily white gum product formed from the purification of the reaction between 4,4'-dimethyl-2,2'-bipyridine with *N*-bromosuccinimide.

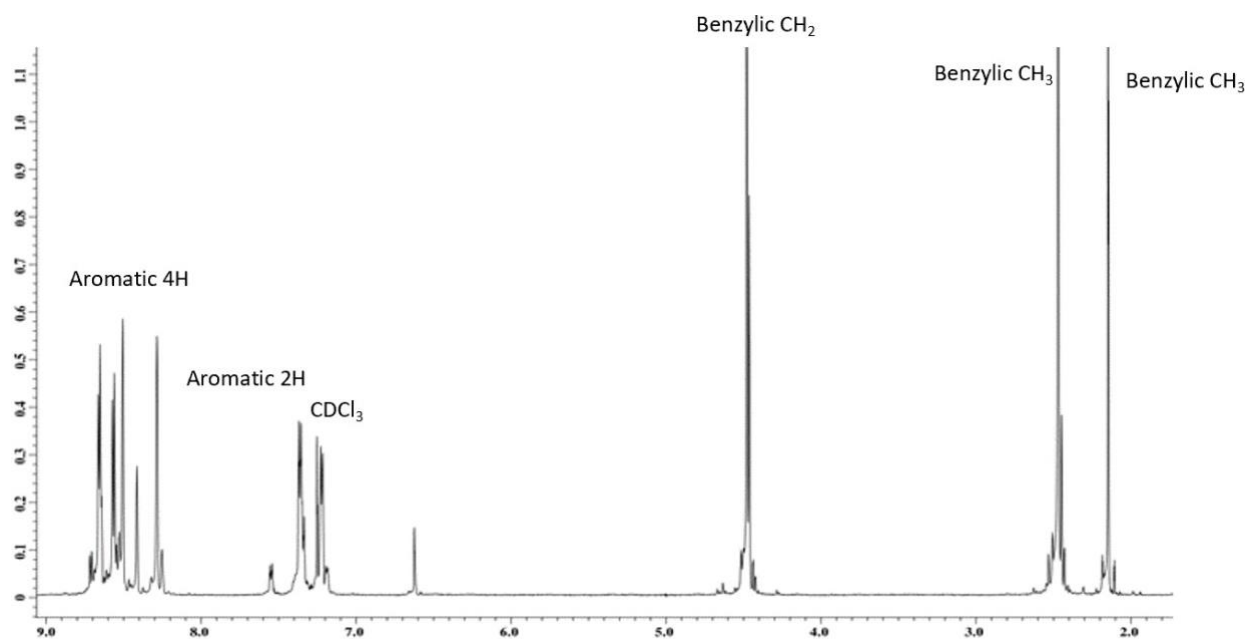


Figure 23. $^1\text{H-NMR}$ of 4-(bromomethyl)-4'-methyl-2,2'-bipyridine in CDCl_3

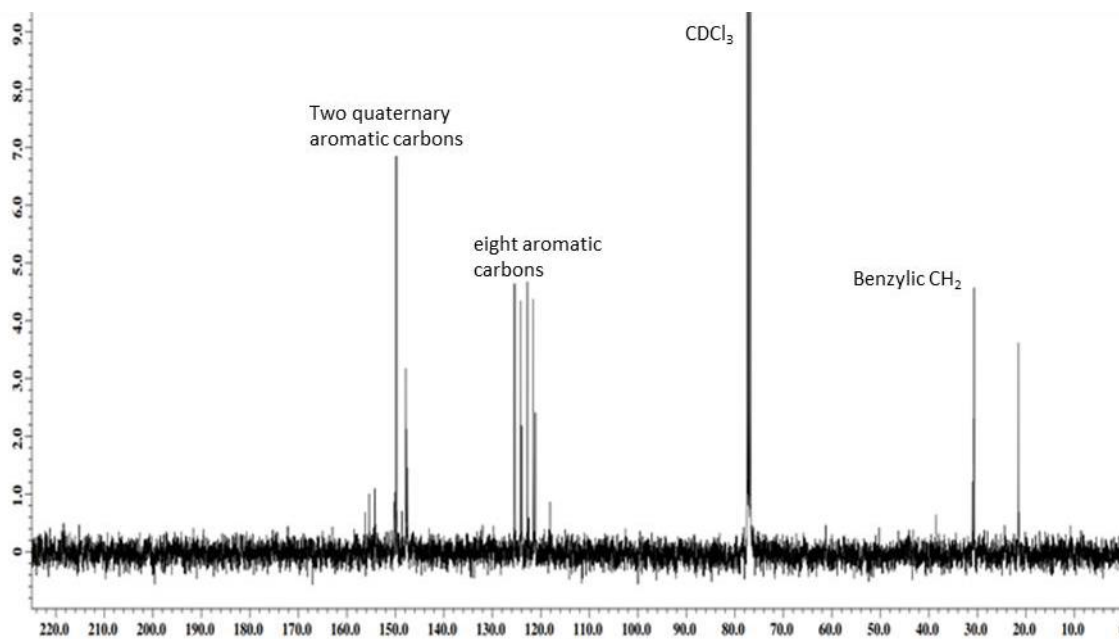


Figure 24. $^{13}\text{C-NMR}$ of 4-(bromomethyl)-4'-methyl-2,2'-bipyridine in CDCl_3

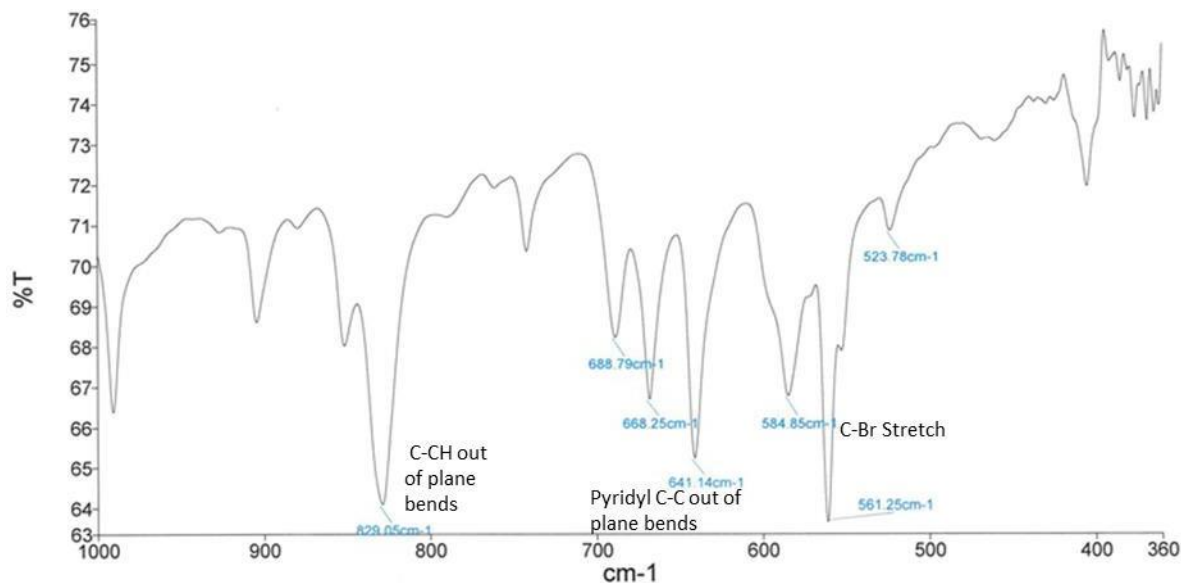


Figure 25. Infrared spectrum of 4-(bromomethyl)-4'-methyl-2,2'-bipyridine. Taken as a KBr pellet from 360cm^{-1} to 1000cm^{-1} .

Synthesis of $[\text{Ru}(4\text{-CH}_2\text{Br-4'-(2,2'-bipyridine)})(2,2'\text{-bipyridine})_2](\text{PF}_6)_2$

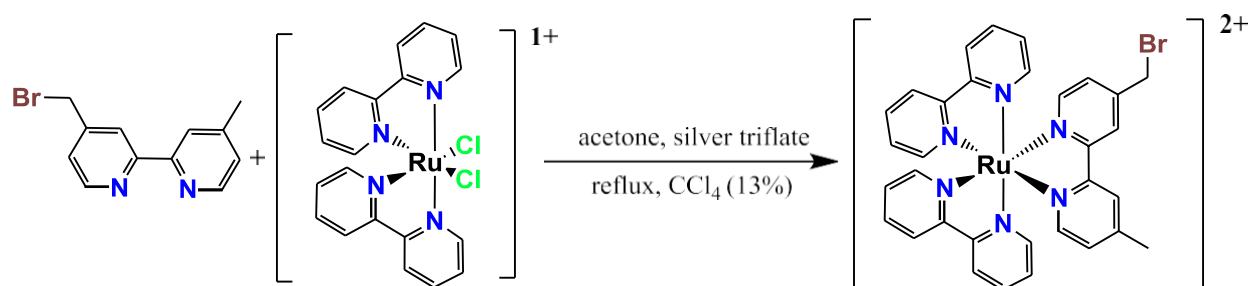


Figure 26. Synthesis of modified tris(bipyridine)ruthenium(II) photosensitizer, $[\text{Ru}(4\text{-CH}_2\text{Br-4'-(2,2'-bipyridine)})(2,2'\text{-bipyridine})_2](\text{PF}_6)_2$.

Over the course of the reaction between $\text{Ru}(\text{bpy})_2\text{Cl}_2$ and silver triflate, a milky white precipitate slowly appeared at the bottom of the reaction flask. This precipitate was successfully filtered out leaving behind a red liquid. The reaction of this liquid with 4-(bromomethyl)-4'-methyl-2,2'-bipyridine obtained from the previous step resulted in a slightly lighter red liquid. Precipitation through the use of excess ammonium hexafluorophosphate resulted in an orange cloudy precipitate

present in solution. This precipitate was successfully filtered out using filter paper and once dried formed a neo orange product with a 13.3% yield. $^1\text{H-NMR}$ spectroscopy and UV-visible spectroscopy data is presented in Figure 27 and 28.

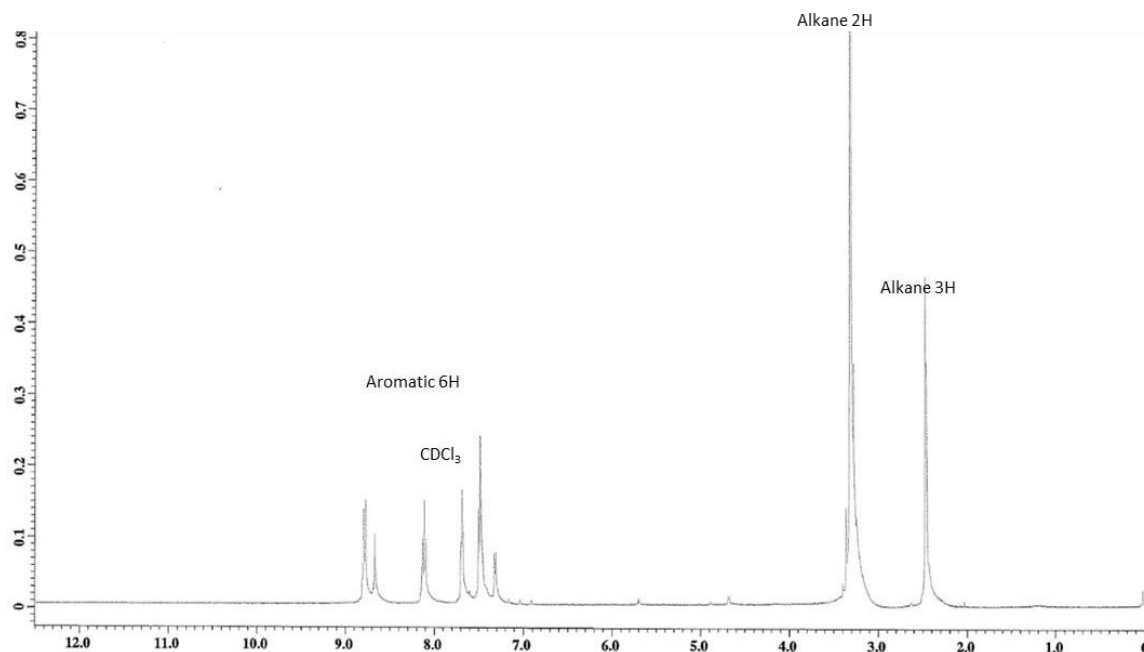


Figure 27 $^1\text{H-NMR}$ spectrum of the brominated tris(bipyridine)ruthenium, $[\text{Ru}(4\text{-CH}_2\text{Br-4'-(2,2'\text{-bipyridine)}(2,2'\text{-bipyridine})_2)(\text{PF}_6)_2]$. NMR experiments utilized deuterated chloroform as a solvent.

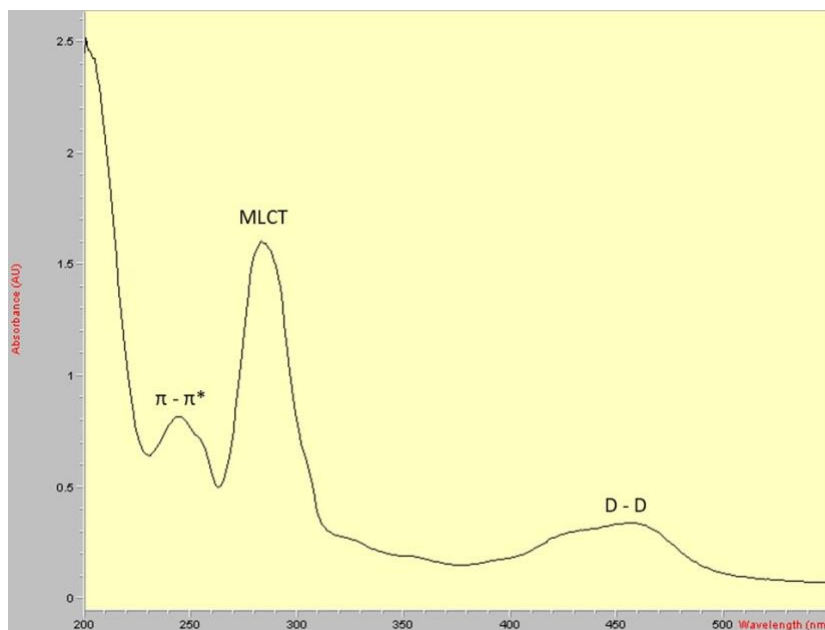


Figure 28. UV-visible spectrum of the brominated tris(bipyridine)ruthenium, $[\text{Ru}(4\text{-CH}_2\text{Br-4'-(2,2'\text{-bipyridine})(2,2'\text{-bipyridine})_2](\text{PF}_6)_2$. The solvent for electronic excitation was deionized water.

Synthesis of the brominated $[\text{Cp}^\text{Ir}(\text{bpy})(\text{Cl})][\text{Cl}]$*

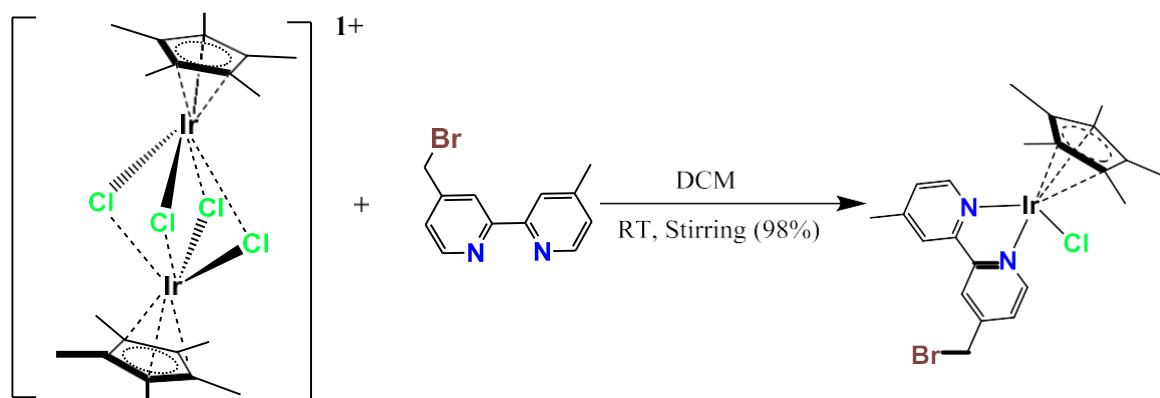


Figure 29. Reaction schematic following the synthesis of $[\text{Cp}^*\text{Ir}(\text{bpy})(\text{Cl})][\text{Cl}]$.

Following dissolution of 4-(bromomethyl)-4-methyl-2,2'-bipyridine and the iridium precursor in DCM, the solution rapidly changed colors from a dark orange to a light yellow. The product easily dried off forming a coating along the glassware and a crude $^1\text{H-NMR}$ and UV-visible spectra were

taken (Figure 30 and Figure 31). 24 hours following vapor diffusion of ether on acetonitrile, thin needle crystals were observed (Figure 32). X-ray diffraction yielded a poor resolution crystal structure of indeterminate accuracy.

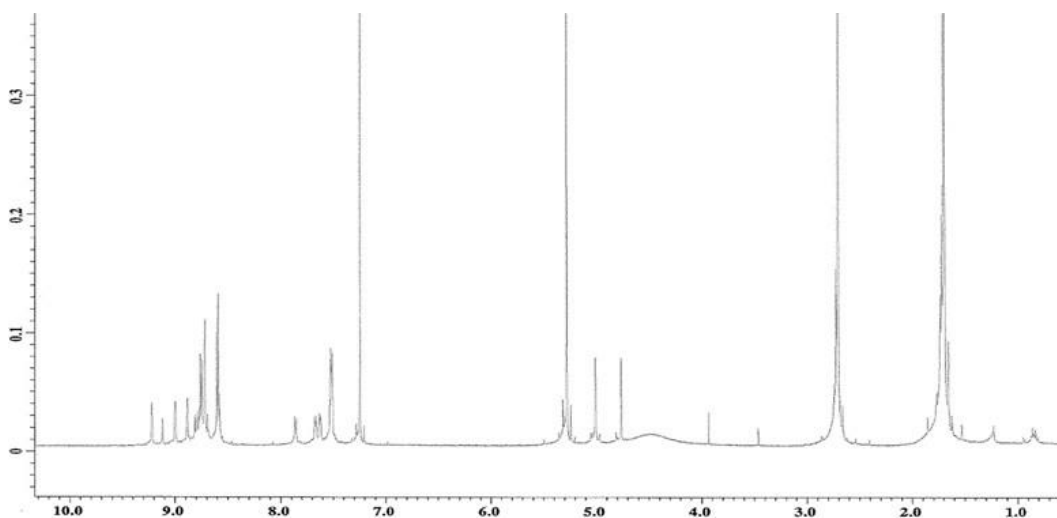


Figure 30. Crude ¹H-NMR spectrum of the brominated [Cp*Ir(bpy)(Cl)][Cl] in deuterated chloroform.

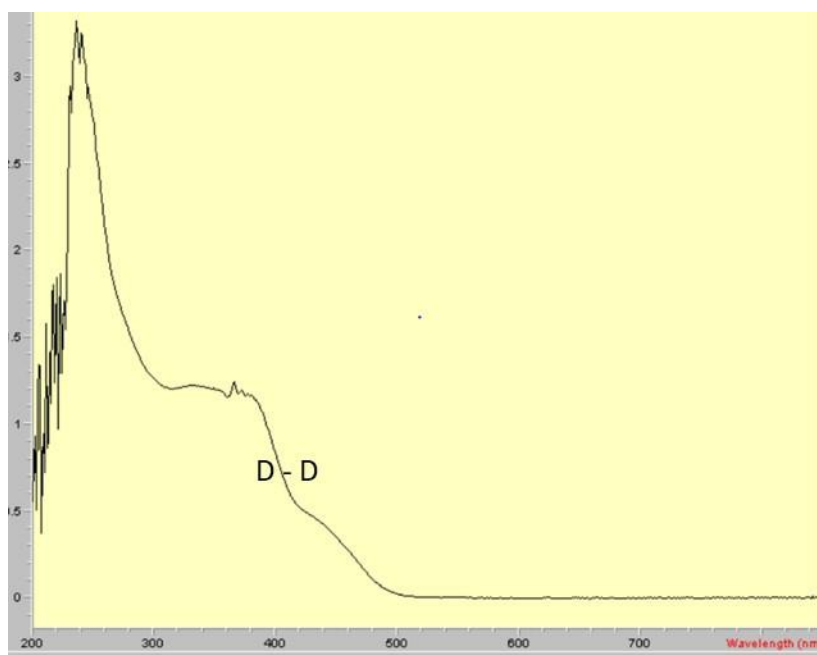


Figure 31. UV-Vis spectra of a minimal amount of brominated [Cp*Ir(bpy)(Cl)][Cl] dissolved in DI water.

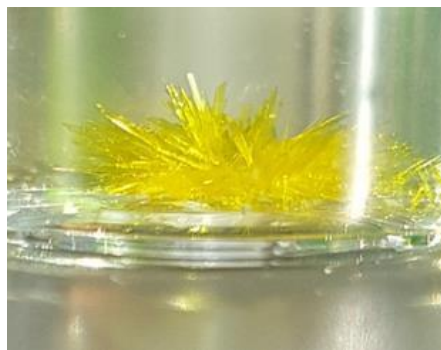


Figure 32. Crystals of $[\text{Cp}^*\text{Ir}(\text{bpy})(\text{Cl})][\text{Cl}]$ obtained following vapor diffusion of diethyl ether on acetonitrile.

Initial GC-TCD Experimentation

The raw thermal conductivity data received from the GC-TCD software is presented in Figure 33, while the standard curve created from the stepwise addition of decreasing amounts of hydrogen gas is presented in Figure 34. Finally, the TCD data received from the GC-TCD software from the addition of 100 μL of headspace from the tris(bipyridine)ruthenium – chloro(pyridine)cobaloxime reaction is presented in Figure 35. Unfortunately, the amount of hydrogen in the sample was beneath the calibration curve and quantification was not possible due to a lack of time to repeat the calibration curve with lower concentration of hydrogen gas.

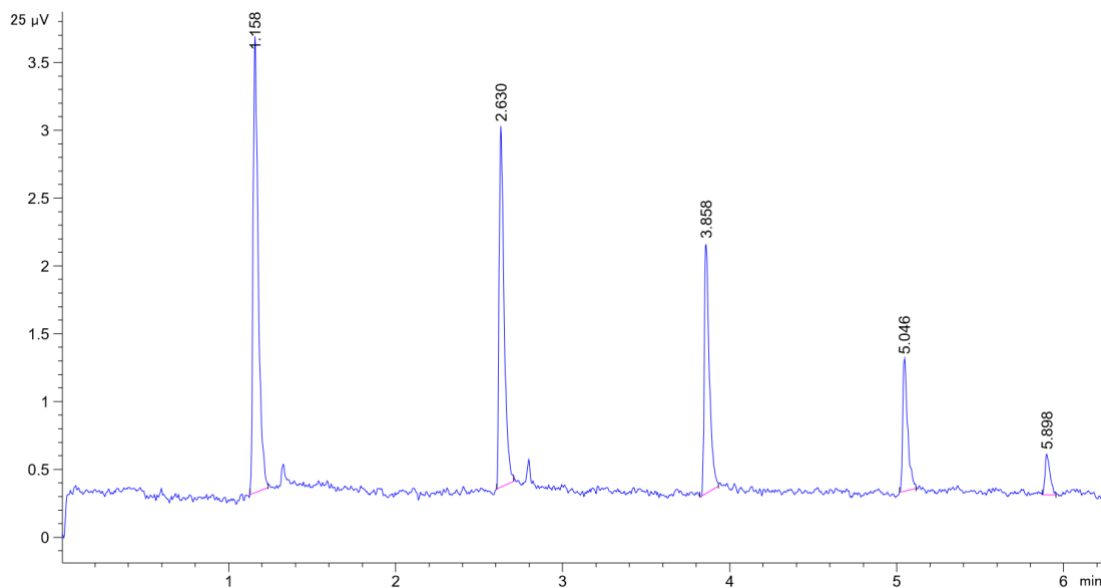


Figure 33. Reverse polarity TCD data received from the GC-TCD after the stepwise addition of decreasing amounts of headspace from the standard sample.

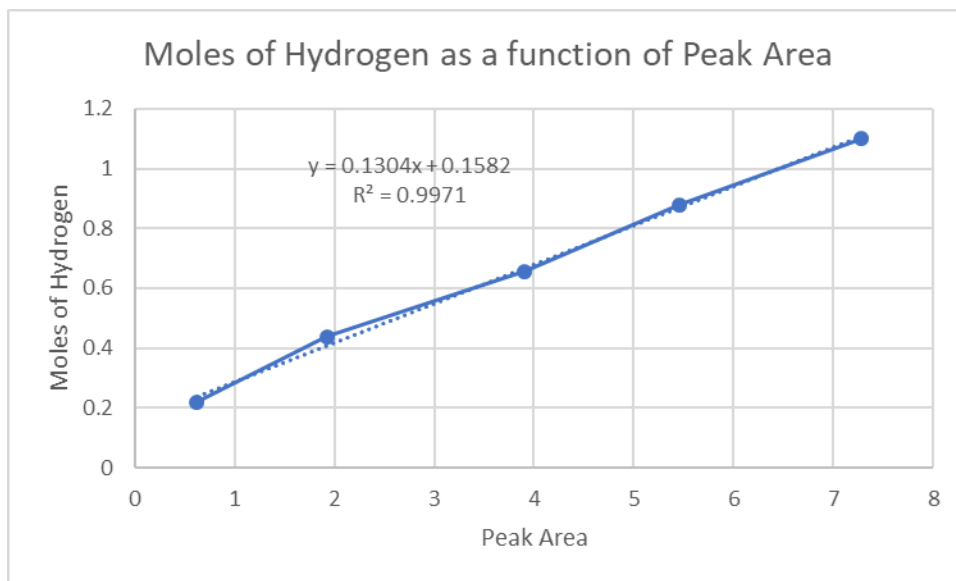


Figure 34. Linear relationship between the volume of injected headspace and mass of hydrogen observed from the standard solution.

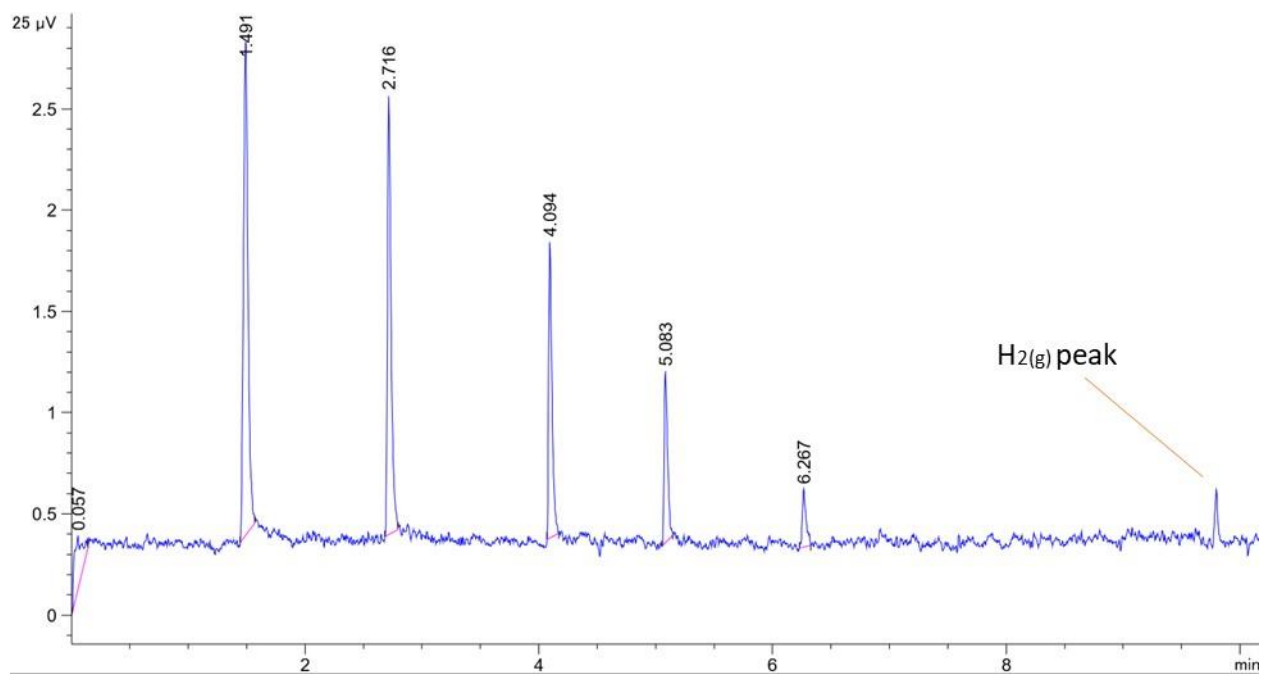


Figure 35. TCD data received from the GC-TCD software from the addition of 100 μL of headspace from the tris(bipyridine)ruthenium – chloro(pyridine)cobaloxime reaction.

Discussion

Digestion of vectors and ligation of gene insert

Based on the fact that the pEM-T vector DNA was cut into two pieces (Figure 21), the size of the pEM-T vector (7,800 base pairs), and the bands position relative to the ladder on the electrophoresis gel, it is reasonable to estimate that the first band present in the second lane is the larger portion of the cut vector. In regard to the cut pET21a(+)-HpDsbG vector containing the rubredoxin insert, the gel shows that lane three containing the cut plasmid contains two distinct bands indicating a successful digestion. Considering the size of the vector insert (195 base pairs), the second band is positioned at a reasonable distance from the point of origin suggesting that this is indeed the rubredoxin insert gene desired. In terms of the ligation of the rubredoxin insert and the vector backbone (Figure 19), the gel shows only one band present in both the lanes containing the ligation reaction indicating the success of the reaction. The concentration of the digestions and ligations throughout this process fell within reasonable levels predicted by past work.¹⁵ It is interesting to note that on all the gels run during this experiment, the bands present in the gel are consistently positioned slightly higher than the position estimated by the ladder. As this is consistent throughout this experiment as well as past experiments it was disregarded when determining the success of the experiment.

Expression of Rubredoxin

Expression of the rubredoxin protein proceeded smoothly resulting in a decent yield of cell pellet (11.35 g). The visible yellow hue present in the concentrated protein sample gives evidence towards the rubredoxin protein successfully integrating the iron into its tertiary structure. The polyacrylamide gel resulting from the SDS gel protein gel electrophoresis shows a very impure and overloaded sample even with regards to the protein fractions purified through the use of the

Ni-NTA column (Figure 23). In the future, purifications of wild-type rubredoxin, as well as future mutated rubredoxin proteins, may require the use of a size exclusion column to remove excess impurities. The concentration of rubredoxin determined by the Bradford assay (55.58mg/mL) is indicated as a reasonable value by literature, however this value may be skewed by the impurities present in the sample.¹⁶

Mutagenesis of Rubredoxin

Mutagenesis of the rubredoxin wild type DNA ended up failing multiple times. Electrophoresis of the digestion reaction occurring after the PCR step has revealed that no non-methylated DNA is present in solution. This combined with the fact that both control samples provided with the mutagenesis kit have shown to be successful indicates that the most likely location of error lies in either the sequence and structure of the mutagenesis primers or an incorrect sequence of rubredoxin DNA. Since this work completed, other members in the lab group have been successful in mutating the rubredoxin protein after a shift to expression in SHuffle cells from New England Biolabs, which are designed to assist in correct protein folding. Expression is currently taking place in a similar manner to the wild type.

Synthesis of 4-(bromomethyl)-4'-methyl-2,2'-bipyridine

As the reaction between 4,4'-methyl-2,2'-bipyridine and *N*-bromosuccinimide proceeded, the color gradually evolved from a white slurry to an orange solution indicating the release of bromide ions. Silica column chromatography of 4-(Bromomethyl)-4'-methyl-2,2'-bipyridine resulted in a large loss of product likely due to overlap between the initial orange fraction and the second product fraction. The ¹H-NMR of this compounds reveals (Figure 23) the presence of three aromatic signal regions (7.0 ppm to 9.0 ppm) corresponding to the three asymmetric aromatic hydrogens, and an

alkane signal around 4.8 ppm corresponding to the benzylic CH₃. Interestingly, there are also two alkane signals around 2.25 ppm likely corresponding to the presence of the benzylic un-brominated CH₃ group as well as a de-brominated CH₂ group. This de-brominated peak is supported by the gradual formation of a red solid in the sample indicating de-bromination occurring over time. The ¹³C-NMR spectrum also reveals two alkane carbons and ten aromatic carbons matching with the predicted structure (Figure 24).

When the infrared spectrum of 4,4'-methyl-2,2'-bipyridine (Figure 25) is compared to the DFT vibration calculation, several pyridyl bends from 688cm⁻¹ to 642cm⁻¹ and a C-Br stretch coupled to several other C-H stretches at 561cm⁻¹ provide consistencies with the structure. Other peaks appear in similarly predicted regions albeit shifted to higher wavenumbers indicating the necessity for a higher level of theory and larger basis set.

Synthesis of the brominated tris(bipyridine)Ruthenium

Synthesis of tris(bipyridine)ruthenium, [Ru(4-CH₂Br-4'-(2,2'-bipyridine) (2,2'-bipyridine)₂] (PF₆)₂, proceeded as described in the results with a surprisingly low percent yield. ¹H-NMR spectroscopy indicates the presence of two alkane peaks and several aromatic peaks providing evidence towards the predicted structure (Figure 27). UV-visible spectroscopy (Figure 28) reveals a region of π to π* transitions (200 – 225 nm), a region of d to d transitions (350-325nm), as well as a metal ligand charge transfer band around 452nm. The ¹H-NMR data, bright red color, and UV-visible data is consistent with literature findings.¹⁹

*Synthesis of the brominated [Cp*Ir(bpy)(Cl)]Cl*

The reaction between 4-(bromomethyl)-4'-methyl-2,2'-bipyridine and dichloro-(pentamethylcyclopentadienyl)-iridium (III) took place surprisingly quickly with a very rapid

color change. It became quickly becomes apparent when the incorrect stoichiometric ratio was provided as the presence of excess ligand yielded a brown and orange product compared to the correct yellow product. Crystallization following workup proceeded smoothly as well. Unfortunately, the crystal structure was poorly resolved to the point where the presence of bromine could not be confirmed. NMR spectroscopy of the compound resulted in what appeared to be a mixture of compounds. This mixture contained identifiable aromatic and alkyl signals suggesting the presence of the correct species but also multiple species in solution perhaps do to degradation of 4-(bromomethyl)-4'-methyl-2,2'-bipyridine prior to ligation (Figure 30). The UV-Visible spectra (Figure 31) indicates the potential presence of two d – d transitions as well as a π to π^* transitions at lower wavelengths consistent with the presence of cyclopentadiene.

Initial GC-TCD Experimentation

The GC-TCD spectrum revealed the presence of a main peak associated with the presence of hydrogen for each injection, and also demonstrated a smaller peak with a slightly higher retention time than hydrogen (Figure 33). This smaller peak is well resolved from the hydrogen peak, disappears in the later injections, and is likely due the presence of atmospheric air in the sample or syringe. The plotted standard curve was largely linear with an R^2 of 0.997 (Figure 34). Unfortunately, the 24 hours hydrogen evolution reaction between tris(bipyridine)ruthenium and chloro(pyridine)cobaloxime did not produce enough hydrogen to reach the lower end of the standard curve (Figure 35). As this reaction was performed at a pH of 7.0, the lower yield is likely due to the decreased presence of protons that not only push the reaction forward but stabilize the catalyst.²⁵ Furthermore, the reaction was not fully saturated with photosensitizer leading to lower electron transfer and subsequent yield. In future work a greater concentration of photosensitizer,

and a lower pH will be utilize along with dilution of the standard solutions to allow for quantification.

Conclusions

The procedures for the mutation and expression of a highly versatile electron transfer protein has been well established and documented using a variety of DNA manipulation and microbiological techniques. The synthesis of a flexible bipyridine ligand has been optimized and applied to the synthesis of a ruthenium and an iridium-based photosensitizer. An efficient and effective method of evaluating hydrogen production has been established with a GC-TCD system. Future work by the group will focus on the attachment of tris(bipyridine)ruthenium and chloro(pyridine)cobaloxime to rubredoxin and characterization of the rate of photocatalytic hydrogen production by GC-TCD. These studies will involve a variety of pH and concentration optimization as discussed above for the free catalyst and photosensitizer systems.

As described previously, PSI has demonstrated significant hydrogen evolution capability when electrostatically attached to hydrogen evolution catalysts.⁴¹⁻⁴³ As previous work indicates the covalent attachment of system components yields increased hydrogen production, future work will focus on the attachment of a series of $[\text{Cp}^*\text{Ir}(\text{bpy})(\text{Cl})][\text{Cl}]$ molecules to PSI to evaluate its potential as a photo-electrocatalyst when conjoined to a large protein photoactive protein.

References

1. Lewis, N. S.; Nocera, D. G., Powering the planet: chemical challenges in solar energy utilization. *Proc Natl Acad Sci U S A* **2006**, *103* (43), 15729-35.
2. Paris Agreement. 2016.
3. Lewis, N. S., Toward Cost-Effective Solar Energy Use. *Science* **2007**, *315* (798), 798-801.
4. Hydrogen Production: Natural Gas Reforming.
<https://www.energy.gov/eere/fuelcells/hydrogen-production-natural-gas-reforming>.
5. Utschig, L. M.; Soltau, S. R.; Tiede, D. M., Light-driven hydrogen production from Photosystem I-catalyst hybrids. *Curr Opin Chem Biol* **2015**, *25*, 1-8.
6. Harris, D. C., *Quantitative Chemical Analysis*. 2007; Vol. 7, p 663.
7. Institute, N. C. Photodynamic Therapy for Cancer. <https://www.cancer.gov/about-cancer/treatment/types/surgery/photodynamic-fact-sheet>.
8. Dolmans, D. E. J. G. J.; Fukumura, D.; Jain, R. K., Photodynamic therapy for cancer. *Nature Reviews Cancer* **2003**, *3*, 380.
9. Lazarides, T.; McCormick, T.; Du, P.; Luo, G.; Lindley, B.; Eisenberg, R., Making hydrogen from water using a homogeneous system without noble metals. *J Am Chem Soc* **2009**, *131* (26), 9192-4.
10. McCormick, T. M.; Han, Z.; Weinberg, D. J.; Brennessel, W. W.; Holland, P. L.; Eisenberg, R., Impact of ligand exchange in hydrogen production from cobaloxime-containing photocatalytic systems. *Inorg Chem* **2011**, *50* (21), 10660-6.
11. Li, Q.; Chen, L.; Lu, G., Visible-Light-Induced Photocatalytic Hydrogen Generation on Dye-Sensitized Multiwalled Carbon Nanotube/Pt Catalyst. *The Journal of Physical Chemistry C* **2007**, *111* (30), 11494-11499.
12. Mou, Z.; Dong, Y.; Li, S.; Du, Y.; Wang, X.; Yang, P.; Wang, S., Eosin Y functionalized graphene for photocatalytic hydrogen production from water. *International Journal of Hydrogen Energy* **2011**, *36* (15), 8885-8893.
13. Liu, X.; Zhao, L.; Lai, H.; Wei, Y.; Yang, G.; Yin, S.; Yi, Z., Graphene decorated MoS₂ for eosin Y-sensitized hydrogen evolution from water under visible light. *RSC Adv.* **2017**, *7* (74), 46738- 46744.
14. Snare, M. J.; Treloar, F. E.; Ghiggino, K. P.; Thistlethwaite, P. J., The photophysics of rhodamine B. *Journal of Photochemistry* **1982**, *18* (4), 335-346.
15. Kubin, R. F.; Fletcher, A. N., Fluorescence quantum yields of some rhodamine dyes. *Journal of Luminescence* **1982**, *27* (4), 455-462.
16. Forster, S.; Thumser, A. E.; Hood, S. R.; Plant, N., Characterization of Rhodamine-123 as a Tracer Dye for Use In In vitro Drug Transport Assays. *Public Library of Science* **2012**, *7* (3), e33253.
17. Soltau, S. R.; Dahlberg, P. D.; Niklas, J.; Poluektov, O. G.; Mulfort, K. L.; Utschig, L. M., Ru-protein-Co biohybrids designed for solar hydrogen production: understanding electron transfer pathways related to photocatalytic function. *Chem Sci* **2016**, *7* (12), 7068-7078.
18. Miessler, G. L.; Fischer, P. J. T., D. A. , *Inorganic Chemistry*. Pearson: Boston, 2014; Vol. 5.
19. Kalyanasundaram, K., Photophysics, photochemistry and solar energy conversion with tris(bipyridyl)ruthenium(II) and its analogues. *Coordination Chemistry Reviews* **1982**, *46*, 159-244.

20. Marco, M.; Cedi, A.; Prodi, L.; Gandolfi, T., *Handbook of Photochemistry*. 2006.
21. Gould, S.; Strouse, G. F.; Meyer, T. J.; Sullivan, B. P., Formation of thin polymeric films by electropolymerization. Reduction of metal complexes containing bromomethyl-substituted derivatives of 2,2'-bipyridine. *Inorganic Chemistry* **1991**, *30* (14), 2942-2949.
22. Soltau, S., Photocatalytic Hydrogen Production by Protein Systems. *Postdoc Journal* **2016**, *4* (9), 3-14.
23. Mauro, M.; Alessandro, A.; Septiadi, D.; Kehr, S.; De Cola, L., *When self-assembly meets biology: Luminescent platinum complexes for imaging applications*. 2014; Vol. 43.
24. Jolly, W. L.; et al., *Inorganic Syntheses - Volume 11*. McGraw-Hill: New York, N.Y., 1968; Vol. 11.
25. Mukherjee, A.; Kokhan, O.; Huang, J.; Niklas, J.; Chen, L. X.; Tiede, D. M.; Mulfort, K. L., Detection of a charge-separated catalyst precursor state in a linked photosensitizer-catalyst assembly. *Physical Chemistry Chemical Physics* **2013**, *15* (48), 21070-21076.
26. Lyon, E. J.; Georgakaki, I. P.; Reibenspies, J. H.; Darensbourg, M. Y., Carbon Monoxide and Cyanide Ligands in a Classical Organometallic Complex Model for Fe-Only Hydrogenase. *Angewandte Chemie International Edition* **1999**, *38* (21), 3178-3180.
27. Helm, M.; Stewart, M., A Synthetic Nickel Electrocatalyst with a Turnover Frequency above 100 000 s⁻¹ for H₂ Production. *ChemCatChem* **2012**, *4* (1), 45-46.
28. Sobczynski, A., Molybdenum disulfide as a hydrogen evolution catalyst for water photodecomposition on semiconductors. *Journal of Catalysis* **1991**, *131* (1), 156-166.
29. Eckenhoff, W. T.; Brennessel, W. W.; Eisenberg, R., Light-Driven Hydrogen Production from Aqueous Protons using Molybdenum Catalysts. *Inorganic Chemistry* **2014**, *53* (18), 9860-9869.
30. Pitman, C. L.; Miller, A. J. M., Molecular Photoelectrocatalysts for Visible Light-Driven Hydrogen Evolution from Neutral Water. *ACS Catalysis* **2014**, *4* (8), 2727-2733.
31. Fihri, A.; Artero, V.; Razavet, M.; Baffert, C.; Leibl, W.; Fontecave, M., Cobaloxime-Based Photocatalytic Devices for Hydrogen Production. *Angewandte Chemie International Edition* **2008**, *47* (3), 564-567.
32. Mulfort, K. L.; Tiede, D. M., Supramolecular cobaloxime assemblies for H₂ photocatalysis: an initial solution state structure-function analysis. *J Phys Chem B* **2010**, *114* (45), 14572-81.
33. Mulfort, K. L.; Utschig, L. M., Modular Homogeneous Chromophore-Catalyst Assemblies. *Acc Chem Res* **2016**, *49* (5), 835-43.
34. Lakadamyali, F.; Reisner, E., Photocatalytic H₂ evolution from neutral water with a molecular cobalt catalyst on a dye-sensitised TiO₂ nanoparticle. *Chemical Communications* **2011**, *47* (6), 1695- 1697.
35. Kandemir, B.; Chakraborty, S.; Guo, Y.; Bren, K. L., Semisynthetic and Biomolecular Hydrogen Evolution Catalysts. *Inorg Chem* **2016**, *55* (2), 467-77.
36. Sano, Y.; Onoda, A.; Hayashi, T., A hydrogenase model system based on the sequence of cytochrome c: photochemical hydrogen evolution in aqueous media. *Chemical Communications* **2011**, *47* (29), 8229-8231.
37. Soltau, S. R.; Niklas, J.; Dahlberg, P. D.; Poluektov, O. G.; Tiede, D. M.; Mulfort, K. L.; Utschig, L. M., Aqueous light driven hydrogen production by a Ru-ferredoxin-Co biohybrid. *Chem Commun (Camb)* **2015**, *51* (53), 10628-31.

38. Soltau, S. R.; Niklas, J.; Dahlberg, P. D.; Mulfort, K. L.; Poluektov, O. G.; Utschig, L. M., Charge Separation Related to Photocatalytic H₂ Production from a Ru–Apoflavodoxin–Ni Biohybrid. *ACS Energy Letters* **2016**, 2 (1), 230-237.
39. Kandemir, B.; Kubie, L.; Guo, Y.; Sheldon, B.; Bren, K. L., Hydrogen Evolution from Water under Aerobic Conditions Catalyzed by a Cobalt ATCUN Metallopeptide. *Inorg Chem* **2016**, 55 (4), 1355-7.
40. Roy, A.; Madden, C.; Ghirlanda, G., Photo-induced hydrogen production in a helical peptide incorporating a [FeFe] hydrogenase active site mimic. *Chemical Communications* **2012**, 48 (79), 9816-9818.
41. Donald Voet, J. V., Charlotte Pratt *Fundamentals of Biochemistry*. John Wiley & Sons: United States of America, 2013; Vol. 4.
42. Utschig, L. M.; Silver, S. C.; Mulfort, K. L.; Tiede, D. M., Nature-driven photochemistry for catalytic solar hydrogen production: a Photosystem I-transition metal catalyst hybrid. *J Am Chem Soc* **2011**, 133 (41), 16334-7.
43. Utschig, L. M.; Dimitrijevic, N. M.; Poluektov, O. G.; Chemerisov, S. D.; Mulfort, K. L.; Tiede, D. M., Photocatalytic Hydrogen Production from Noncovalent Biohybrid Photosystem I/Pt Nanoparticle Complexes. *The Journal of Physical Chemistry Letters* **2011**, 2 (3), 236-241.
44. Bunker, B.; Stern, E. A., The iron-sulfur environment in rubredoxin. *Biophysical journal* **1977**, 19 (3), 253-264.
45. Prakash, S.; Sundd, M.; Guptasarma, P., The key to the extraordinary thermal stability of P. furiousus holo-rubredoxin: iron binding-guided packing of a core aromatic cluster responsible for high kinetic stability of the native structure. *PloS one* **2014**, 9 (3), e89703-e89703.
46. Maiti, B. K.; Almeida, R. M.; Moura, I.; Moura, J. J. G., Rubredoxins derivatives: Simple sulphur-rich coordination metal sites and its relevance for biology and chemistry. *Coordination Chemistry Reviews* **2017**, 352, 379-397.
47. Slater, J. W.; Shafaat, H. S., Nickel-Substituted Rubredoxin as a Minimal Enzyme Model for Hydrogenase. *J Phys Chem Lett* **2015**, 6 (18), 3731-6.
48. Fitzgerald, M. P.; Rogers, L. J.; Rao, K. K.; Hall, D. O., Efficiency of ferredoxins and flavodoxins as mediators in systems for hydrogen evolution. *The Biochemical journal* **1980**, 192 (2), 665-672.
49. Swinehart, D. F., The Beer-Lambert Law. *Journal of Chemical Education* **1962**, 39 (7), 333.
50. Hanwell, M. D.; Curtis, D. E.; Lonie, D. C.; Vandermeersch, T.; Zurek, E.; Hutchison, G. R., Avogadro: an advanced semantic chemical editor, visualization, and analysis platform. *Journal of Cheminformatics* **2012**, 4 (1), 17.